**Experience-dependent reorganization drives the development of a binocularly unified representation of orientation in ferret visual cortex**

**David Whitney[1,2], Jeremy T. Chang[1,2], David Fitzpatrick[1,*]**

1. Department of Functional Architecture and Development of Cerebral Cortex, Max Planck Florida Institute for Neuroscience, Jupiter, Florida, USA.

2. These authors contributed equally to this work.

*Correspondence should be addressed to David Fitzpatrick (david.fitzpatrick@mpfi.org)

**Keywords:** visual cortex, orientation, binocular, development, ferret, reorganization

**Abstract**

Across sensory areas, neural microcircuits consolidate diverse streams of sensory information into unified, representations of the external world, but the developmental process underlying alignment of sensory representations remains poorly understood. Using two-photon and widefield epifluorescence calcium imaging in developing ferret visual cortex, we find an early developmental period in which monocular stimulation reveals two divergent representations of orientation at the network and cellular-scales. During the period of monocular network misalignment, binocular stimulation drives a third orientation representation, distinct from the constituent monocular representations. Alignment towards a single, binocularly unified representation requires binocular visual experience shortly after eye-opening. Chronic imaging demonstrates that the monocular and binocular orientation representations functionally reorganize towards a single representation resembling the early binocular representation through concerted shifts in preferred orientation across the cellular-scale and network-scale representations. Thus, we propose that an experience-dependent learning process drives the emergence of a unified binocular representation of orientation.

## Introduction

A significant step towards mature sensory processing is the developmental emergence of comprehensive neural representations of an organism's environment. To achieve this, neural circuits combine information from different sensory sources to generate unified unisensory or multisensory representations (Duhamel et al., 1998; King and Hutchings, 1987; Knudsen and Brainard, 1991; Wallace and Stein, 1997). The binocular and monocular representations of stimulus orientation in visual cortex provide an excellent example of this integrative process (Bridge and Cumming, 2001; Crair et al., 1998; Wang et al., 2010). Segregated inputs from the two eyes first come together in the visual cortex to yield a unified binocular representation of stimulus orientation, such that visual stimuli presented to either eye yield similar orientation selective responses(Bridge and Cumming, 2001; Sarnaik et al., 2014).

Previous studies, however, have failed to reach consensus on the developmental process that forms a unified binocular representation. Electrophysiological studies in mice have found monocular differences in the preferred orientation of individual cortical neurons early in development, and demonstrated that sensory experience is necessary to achieve matched orientation preferences(Gu and Cang, 2016; Wang et al., 2010). But studies of the more complex visual systems of carnivores and primates, where neuronal orientation preferences spatially cluster into a smoothly varying columnar representation, have reached different conclusions. Here the representation of preferred orientation is generally viewed as innately determined, independent of experience (Chapman et al., 1996; Crair et al., 1998; Godecke and Bonhoeffer, 1996; Sengpiel et al., 1998; Wiesel and Hubel, 1974). Moreover, studies in kittens using intrinsic signal imaging failed to find orientation preference mismatches, suggesting that an aligned layout for stimulus orientation is prespecified (Crair et al., 1998; Godecke and Bonhoeffer, 1996). Together these results open up the possibility

that different developmental processes underlie the emergence of matched orientation representations in rodents and carnivores (Cang and Feldheim, 2013).

In this study, we examined the development of the unified binocular representation of orientation at network- and cellular-scales using widefield and two-photon calcium imaging in ferret visual cortex, a species with a well-developed columnar architecture. At eye-opening, individual neurons exhibit interocular mismatches in preferred orientation for neurons that manifests in misaligned network-wide, representations of orientation for each eye. Furthermore, synaptic inputs underlying these nascent monocular representations interact to generate a binocular representation that is not trivially related to either monocular representation. During the first week following eye-opening, patterned visual experience drives the functional reorganization of both monocular representations towards the early binocular representation. We propose that the emergence of a binocularly aligned orientation representation in visual cortex reflects a process of experience-driven alignment across network-scale representations.

## Results

### Mismatched monocular orientation preference is reduced across development

To measure monocular orientation preferences in the ferret visual cortex, we utilized viral expression of GCaMP6s with widefield epifluorescence imaging (Figure 1A-B). In ferrets, neurons first become orientation selective around eye-opening (~P30) and reach mature levels within one week (Chapman and Stryker, 1993; Chapman et al., 1996; Clemens et al., 2012; White et al., 2001). We first investigated the similarity of trial-averaged activity patterns evoked by drifting square wave gratings presented to either eye in visually experienced animals (experienced, P36-42, Figure 1A,C). Activity patterns evoked by the same stimulus orientation were well matched between the eyes (Supplemental Figure 1A-C) and produced a binocularly unified representation of orientation

preference (Figure 1D). We next examined orientation-specific responses in visually naive animals prior to natural eye-opening (naive, P27-31, Figure 1A). In visually naive animals, stimuli presented to each of the opened eyes evoked distinct patterns of trial-averaged population activity (Figure 1E-F, Supplemental Figure 1D-F, Pearson's correlation: Naive r=0.31±0.09 vs Experienced r=0.79±0.03 (Mean±SEM), n=6 vs 7 animals, p<0.001, unpaired permutation test), resulting in a higher monocular mismatch of preferred orientation than is observed in experienced animals (Figure 1G, Mean monocular mismatch: Naive 27.91±4.19˚ vs Experienced 11.04 ±1.57˚ (Mean±SEM), n=6 vs 7 animals, p<0.001, unpaired permutation test). We failed to account for the monocular mismatch in naive animals with any rotational transform of the widefield orientation preferences, suggesting that monocular mismatch is cortical in origin and not due to physical torsion on the eyes (Supplementary Figure 1G-I, minimum monocular mismatch after allowing rotation: Naive 25.19±4.55˚ vs Experienced 9.23±1.03˚ (Mean±SEM), n=6 vs 7 animals, p<0.001, unpaired permutation test).

Monocularly mismatched orientation preferences at the level of widefield epifluorescence imaging could arise from the coordinated activity within cortical networks in two possible scenarios. First, the ipsilateral and contralateral responses could reflect two distinct, but spatially intermingled neural populations, in which individual neurons predominantly respond to visual input from a single eye. Alternatively, neurons could be binocularly responsive, but display monocularly mismatched orientation preferences. To test these two possibilities, we used two-photon calcium imaging to measure responses to oriented stimuli in layer 2/3 (L2/3) pyramidal neurons of visual cortex in both naive and experienced animals (Figure 1A-B). We discovered that most recorded neurons were binocularly responsive (Figure1H-I, Fraction of binocularly responsive cells: Naive 100±0% vs Experienced 96.27±1.57% (Mean±SEM), n=3 animals), but binocularly responsive

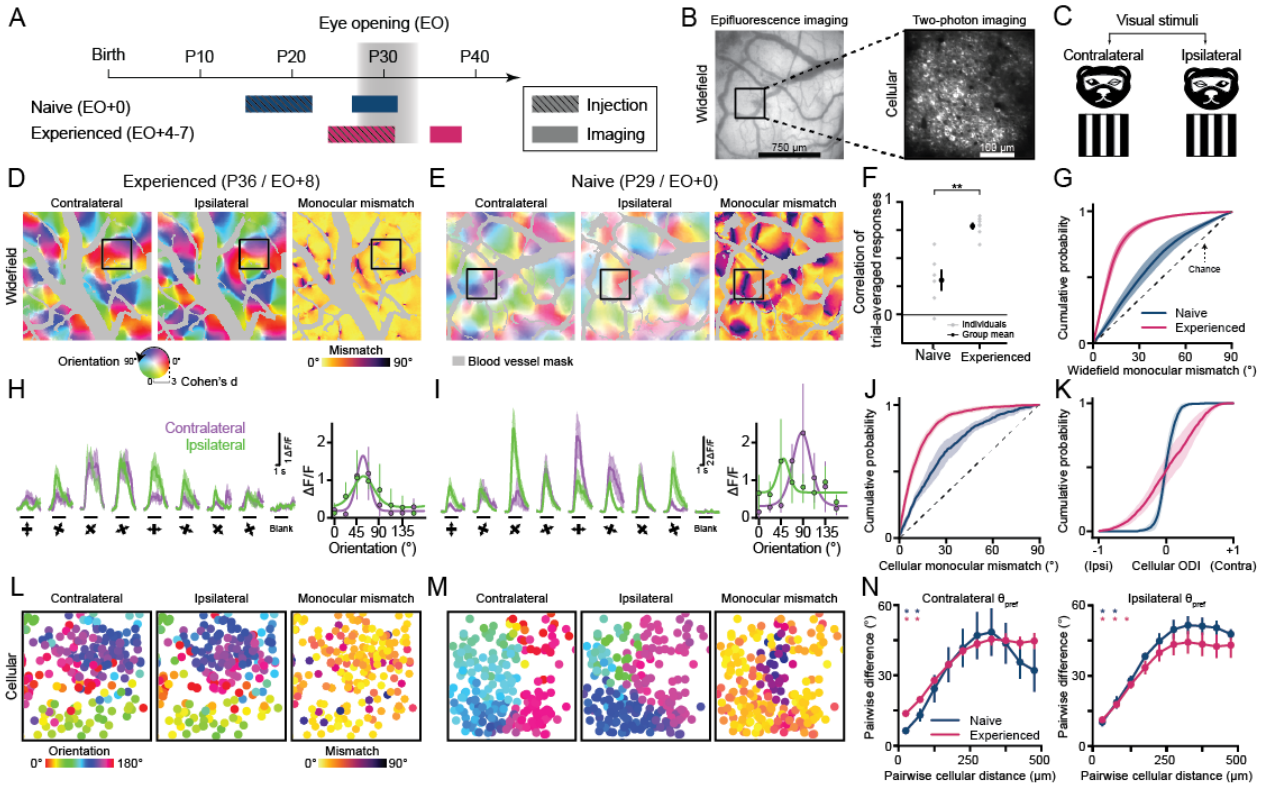


**Figure 1: Mismatched monocular orientation preference is reduced across development. (A)** Experimental timeline. **(B)** Representative widefield and two-photon images from the naive animal in (E). **(C)** Schematic of visual stimulation. **(D-E)** Representative widefield, monocular orientation preference maps for experienced animals (D) and naive animals (E). Far right column is monocular mismatch and grayed out regions represent blood vessels. Preferred orientation and selectivity (or monocular mismatch) are represented respectively by image hue and saturation (or image color). **(F)** Pearson's correlation between monocular trial-averaged responses. Gray and black dots respectively reflect individual or grouped measurements. **(G)** Cumulative distributions of widefield monocular mismatch for naive and experienced animals (mean±SEM). **(H-I)** Representative cellular response traces (left panel, mean±SEM) and orientation tuning curves fit to trial-averaged responses (right panel, median±MAD) for experienced (H) and naive (I) animals. The solid black line under each response trace indicates when the visual stimulus was presented. **(J-K)** Cumulative distributions of cellular monocular mismatch (J) and ocular dominance index (K) for naive and experienced animals (mean±SEM). **(L-M)** Cellular monocular orientation preference maps (and monocular mismatch maps) for the boxed regions in (D) and (E). Circles are cells and color represents either the preferred orientation or monocular mismatch. **(N)** Distance-dependent, cellular clustering of the monocular preferred orientation for naive and

experienced animals (mean±SEM). Scale bars for widefield imaging and two-photon in (B) apply to (D-E, L-M). Asterisks denote significance between groups in (F) and distances where clustering is significant in (**N**) (*: $p<0.05$, **:$p<0.01$). Animal experiments: naive (n=3 cellular and n=6 widefield) and experienced (n=3 cellular and n=7 widefield).

neurons in naive animals often displayed mismatched orientation preferences, whereas they were well matched in experienced animals (Figure 1J, Supplementary Figure 2, Mean monocular mismatch: Naive 26.87±2.90˚ vs Experienced 13.11±1.03° (Mean±SEM), n=3 animals, p=0.002, unpaired bootstrap test). Furthermore, binocularly responsive neurons from naive animals did not yet display stronger responses to monocular stimulation like experienced animals (Figure 1K, ODI: Naive 0.05±0.03 vs Experienced 0.23±0.06 (Mean±SD), Monocularity: Naive 0.09±0.04 vs Experienced 0.47±0.09 (Mean±SD), n=3 animals, p=0.04 for ODI and p=0.01 for Monocularity, unpaired bootstrap test) suggesting that ocular dominance only becomes pronounced after eye opening. Taken together, our results demonstrate that cortical neurons at eye-opening are binocularly responsive and frequently exhibit monocular mismatches in orientation preference that then become reduced during the first week of visual experience.

Weaker orientation selectivity in naive animals could contribute to the apparent orientation preference mismatches. To rule out the contribution of weak orientation selectivity, we limited analysis to binocularly responsive neurons and pixels that exhibited well-tuned orientation responses (Fraction of well-tuned cells: Naive 56.76±3.94% vs Experienced 71.32±7.75% (Mean±SEM), n=3 animals; Fraction of well-tuned pixels: Naive 35.54±4.64% vs Experienced 80.87±2.33% (Mean±SEM), n=6 vs 7 animals). Furthermore, we evaluated whether the observed monocular mismatch could be accounted by measurement error of the preferred orientation. By bootstrap resampling the preferred orientation, we calculated the worst-case measurement error of

the preferred orientation for either contralateral or ipsilateral stimulation. The observed monocular mismatch in naive animals was higher than the bootstrapped measurement error for either eye (Bootstrapped measurement error for cells: Naive contralateral 13.64˚ and ipsilateral 20.89˚, Experienced contralateral 12.21˚ and ipsilateral 12.34˚, n=3 animals; Bootstrapped measurement error for pixels: Naive contralateral 10.23±0.68˚ and ipsilateral 12.31±0.56˚, Experienced contralateral 8.24±0.55˚ and ipsilateral 7.38±0.45˚ (Mean±SEM), n=6 or 7 animals). Therefore, unreliable or weak orientation selectivity cannot explain the observed orientation preference mismatches.

In the mature visual cortex, neurons that share similar orientation preferences are spatially clustered, defining a modular, but spatially distributed columnar representation of orientation across visual cortex (Figure 1D, Supplementary Figure 1A-C). The modular patterns evident in the trial-average population responses of naive animals visualized with widefield epifluorescence imaging (Supplementary Figure 1D-F) suggest that cells might already spatially cluster by monocular preferred orientation (Figure 1L-M). To test this possibility, we quantified the spatial clustering by computing the cellular pairwise difference in preferred orientation as a function of distance for stimulation to each eye. Naive animals did not display a higher degree of local scatter in preferred orientation than experienced animals (Figure 1N, $p<0.05$ within 100μm unpaired bootstrap test for both Naive and Experienced), consistent with the early columnar organization that has been visualized for spontaneous activity (Smith et al., 2018). Thus, we conclude that hallmarks of the mature visual cortex, such as orientation selectivity, binocular responsiveness, and a columnar architecture, are each already present in visually naive ferrets. Yet despite this unexpected degree of functionalization to network organization, differences in monocular orientation preference are observable before eye-opening.

**Topologically distinct monocular orientation representations before eye-opening**

We next sought to reconcile our observations that monocular orientation preferences are spatially organized, yet display monocular mismatch. The presence of monocular mismatch within a cortical network displaying a fine-scale spatial clustering for the stimulus orientation of each eye raises the possibility that early binocular cortical networks harbor distinct modular representations of orientation for each eye, which are systematically misaligned in their preferred orientation (Figure 2A-C). To quantify whether the spatial layout of the preferred orientation is different for the monocular representations in naive animals, we computed the circular correlation of the monocular preferred orientations using widefield imaging. Consistent with our hypothesis, we found that the circular correlation of monocular preferred orientations was substantially lower in naive animals indicating that the monocular representations are distinct (Figure 2D, Circular correlation of monocular preferred orientations: Naive: $r=0.44\pm0.11$ vs Experienced: $r=0.87\pm0.03$ (Mean±SEM), n=6 vs 7 animals, $p<0.001$, unpaired permutation test). If the monocular mismatch does arise from distinct monocular representations, the spatial structure of the evoked response and the location of fine-scale topological features of monocular orientation preference maps, such as pinwheel centers and linear fractures, are unlikely to be shared. Because regions of low-homogeneity reflect pinwheels and linear fractures, we compared the homogeneity index (HI), which measures the local similarity of orientation preference within 100μm, for monocular orientation preference maps obtained with widefield imaging. Consistent with our hypothesis, we observed that the fine-network structures of the monocular representations, as assessed by HI, were less similar in naive animals than in experienced animals (Figure 2C,E, Pearson's correlation of monocular HI: Naive: $r=0.41\pm0.11$ vs Experienced: $r=0.74\pm0.03$ (Mean±SEM), n=6 vs 7 animals, $p<0.001$, unpaired permutation test).

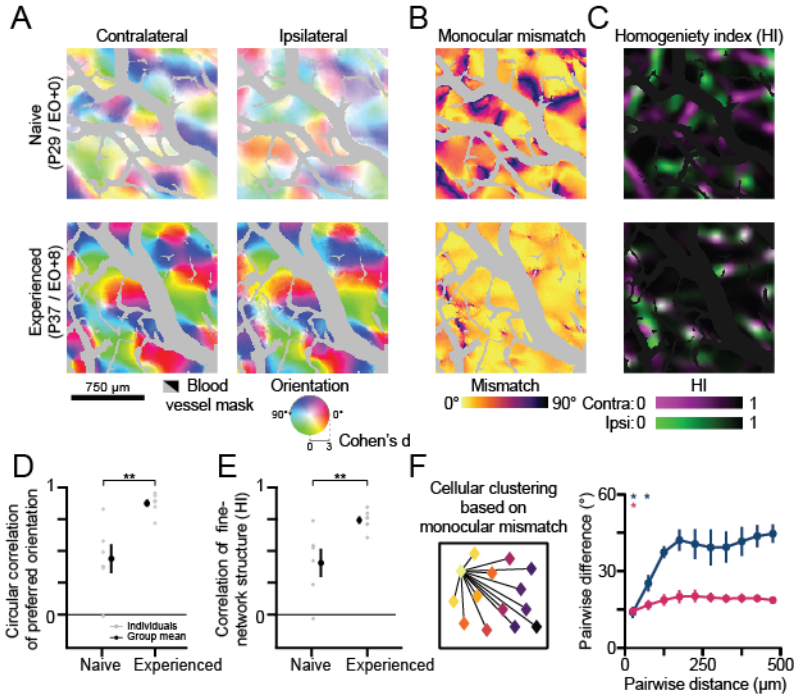


**Figure 2: Monocular orientation representations are distinct before eye-opening.**

**(A)** Representative widefield, monocular maps of orientation preference for naive animals (top row) and experienced animals (bottom row). Preferred orientation and selectively are respectively represented by image hue and saturation. Grayed or blacked out regions represent blood vessels. **(B-C)** Monocular mismatch (B) and homogeneity index maps (C) for the monocular orientation preference maps in (A). **(D-E)** Circular correlation of preferred orientation for monocular orientation preference maps (D) and Pearson's correlation of fine-network structure (homogeneity index) for monocular orientation preference maps (E) for naive and experienced animals (mean±SEM). Gray and black dots respectively reflect individual or grouped measurements. **(F)** Distance-dependent, cellular clustering of the monocular mismatch for naive and experienced animals (mean±SEM). Asterisks denote significance between groups in (D-E) and distances where clustering is significant in (F) (*: $p<0.05$, **:$p<0.01$). Animal experiments: naive (n=3 cellular and n=6 widefield) and experienced (n=3 cellular and n=7 widefield).

An important prediction of two distinct monocular columnar representations is the presence of clustered hotspots of orientation preference mismatch. To test this hypothesis, we calculated the difference in observed monocular mismatch for pairs of cells as a function of distance. We

observed that cells from naive animals displayed significant clustering of monocular mismatch in a region within 100µm (Figure 2F). Additionally, we failed to find a higher negative correlation between a neuron's orientation selectivity and monocular mismatch in Naive animals (Pearson's correlation between lowest monocular orientation selectivity versus monocular mismatch: Naive: r=-0.371±0.025 vs Experienced r=-0.317±0.017), indicating that the spatial clustering of monocular mismatch is not reflective of cortical regions developmentally ahead. Instead, regions of monocular mismatch appear to be a natural repercussion of misaligned columnar orientation representations. Together our findings suggest that innate factors establish distinct monocular representations of orientation, each representation exhibiting unique topological structure, within the modularly, distributed cortical networks of visual cortex before eye-opening.

**Network-scale alignment of orientation representations requires patterned visual experience**

Since the preferred orientation is matched during the first week after eye-opening, we investigated whether the matching of the preferred orientation requires patterned visual experience. While previous experiments demonstrated that dark rearing and monocular deprivation impair monocular matching in mice(Wang et al., 2010), we sought to disrupt interocular correlations, while also preserving equal visual drive to both eyes. Therefore, we employed binocular eyelid suturing in a cohort of animals to delay eye-opening, depriving animals of normal patterned experience (deprived, P35-36, Figure 3A). Neurons from deprived animals demonstrated higher monocular mismatches in orientation preference than experienced animals (Figure 3B-D, Deprived 37.75±2.43° vs Experienced 13.11±1.03° (Mean±SEM), n=3 animals, p=.008, unpaired bootstrap test). Consistent with previous binocular deprivation studies (Chapman and Stryker, 1993; White et al., 2001), we also found that orientation selectivity in L2/3 neurons from deprived animals was

lower than from experienced animals (Figure 3E, $p<0.05$, unpaired bootstrap tests). Thus, early patterned visual experience plays a dual role in the alignment of the monocular representations and the proper maturation of orientation selectivity.

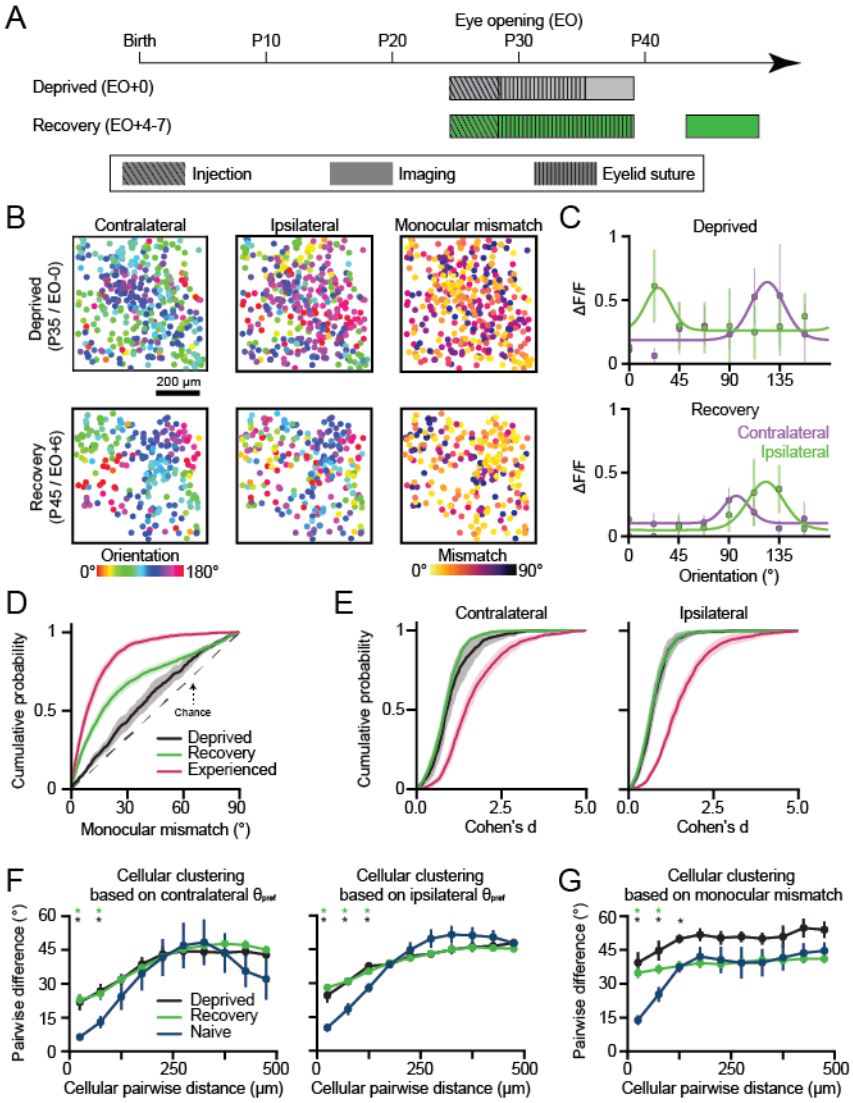


**Figure 3: Network-scale alignment of orientation representations requires patterned visual experience.**

**(A)** Experimental timeline for deprivation and recovery. **(B)** Representative cellular, monocular orientation preference maps and monocular mismatch maps for deprived animals (top row) and recovery animals (bottom row). Circles are cells and color represents either the preferred orientation or monocular mismatch. **(C)** The trial-average response (median±MAD) and fit orientation tuning curves for representative cells from either a deprived animal (top row) or

recovery animal (bottom row). **(D)** Cumulative distribution of cellular monocular mismatch for experienced, deprived, and recovery animals (mean±SEM). **(E)** Cumulative distributions of monocular orientation selectivity (Cohen's d) for experienced, deprived, and recovery animals (mean±SEM). **(F)** Distance-dependent, cellular clustering of the preferred orientation for monocular stimulation in naive, deprived, and recovery animals (mean±SEM). **(G)** Distance-dependent, spatial clustering of monocular mismatch for naive, deprived, and recovery animals (mean±SEM). Asterisks in (F-G) denote distances where clustering is significant (*: $p<0.05$). Animal experiments: deprived (n=3), recovery (n=5), naive (n=3), and experienced (n=5).

Next, we investigated whether patterned visual experience during the first normal week of experience (P30-P37) is critical for producing a binocularly aligned orientation representation. In a cohort of animals, we delayed eye-opening by 9 days with binocular eyelid suturing, and then provided 4-7 days of patterned visual experience (recovery, P43-46, Figure 3A). Notably, recovery animals displayed deficits despite access to comparable amounts of patterned visual experience as normally reared animals. Neurons from recovery animals displayed lower levels of orientation mismatch than from deprived animals (Figure 3B-D, Recovery 27.00±1.43° vs Deprived 37.75±2.43° (Mean±SEM), n=5 vs 3 animals, $p<0.05$, unpaired bootstrap test), but orientation mismatches were significantly higher than from experienced animals (Figure 3D, Recovery 27.00±1.43° vs Experienced 13.11±1.03° (Mean±SEM), n=5 vs 3 animals, $p<0.05$, unpaired bootstrap test). Furthermore, cellular orientation selectivity in the recovery animals was indistinguishable from deprived animals (Figure 3E, $p>0.05$, unpaired bootstrap tests). Therefore, we conclude that early visual experience, during the first week after natural eye-opening, plays an important role in the development orientation selectivity and the alignment of binocular preferences, which cannot be recovered through comparable experience at a later developmental time point.

In addition to single-cell impairments, we discovered that the monocular representations of deprived and recovery animals showed systematically higher local scatter in preferred orientation than naive animals (Figure 3F-G, $p<0.05$ within 100μm unpaired bootstrap test vs Naive). Weakened spatial clustering implies that abnormal closed-eye experience after P30 induces a dramatic transformation of the representational network-structure in ferret visual cortex: from the modular functional organization characteristic of carnivores and primates into a more scattered functional organization reminiscent of the salt-and-pepper organization present in rodents. Alteration to circuit-level representations by abnormal experience is consistent with the underlying cortical circuitry becoming susceptible to visual experience at critical period onset (~P30-P35)(Issa et al., 1999). We therefore conclude that the transition from closed-eye visual experience to patterned vision at ~P30 is critically important for both the proper maintenance of spatially-clustered, columnar representations of orientation and the binocular alignment of preferred orientation.

**Binocular stimulation yields a third orientation representation before eye-opening**

Cortical sensitivity to early visual experience raises the possibility that binocular experience, through simultaneous engagement of synaptic inputs from both eyes, plays a crucial role in establishing an aligned representation of orientation preference. But separate monocular representations of orientation preference could lead to binocularly-driven activity that is weaker or fundamentally different from monocularly-driven activity. Because of the potential importance of binocularly-driven activity, we asked how the cellular-scale and network-scale responses evoked by binocular presentation of drifting gratings would compare with those evoked by monocular presentation (Figure 4A). Thus, we recorded responses to binocular and monocular

stimulation using both two-photon (Figure 4B-E) and widefield (Figure 4F-G) calcium imaging in naive and experienced animals. As expected in experienced animals, the monocular and binocular cellular orientation preferences (Figure 4H-I, Mean orientation preference difference with binocular: Contralateral 10.44±1.10˚, Ipsilateral 12.73±0.40˚ (Mean±SEM), n=3 animals) and network-scale orientation representations were well-matched (Figure 4J-K, Circular correlation with binocular: Contralateral r=0.93±0.01, Ipsilateral: r=0.93±0.02; Pearson's correlation of homogeneity index with binocular: Contralateral: r=0.77±0.03, Ipsilateral: r=0.76±0.05 (Mean±SEM), n=7 animals).

In contrast, binocular stimulation in naive animals drove robust orientation selective responses (Figure 4B-C), but the binocular preferred orientation frequently differed from the monocular preferred orientations in neurons where the monocular mismatch was high (Figure D-E, H-I). Systematic differences in the binocular and monocular preferred orientations in naive animals could result from the co-activation of differently tuned monocular inputs leading to a degraded binocular representation in regions of high monocular mismatch. Signatures of a degraded binocular representation include reduced binocular orientation selectivity and spatial clustering of preferred orientation. Contrary to these predictions, spatial clustering of the binocular preferred orientation was comparable between naive and experienced animals (Supplementary Figure 3A, $p<0.05$ within 100μm for Naive and Experienced, unpaired bootstrap test), and smoothly mapped across the cortex for both the cellular-scale (Figure 4D) and network-scale representations (Figure 4E). Furthermore, at the cellular-scale, we failed to find any systematic difference between binocular and monocular orientation selectivity in either naive or experienced animals (Supplementary Figure 3B, $p>0.05$ for all comparisons, paired bootstrap test), and binocular orientation selectivity was only weakly correlated to the amount of monocular mismatch

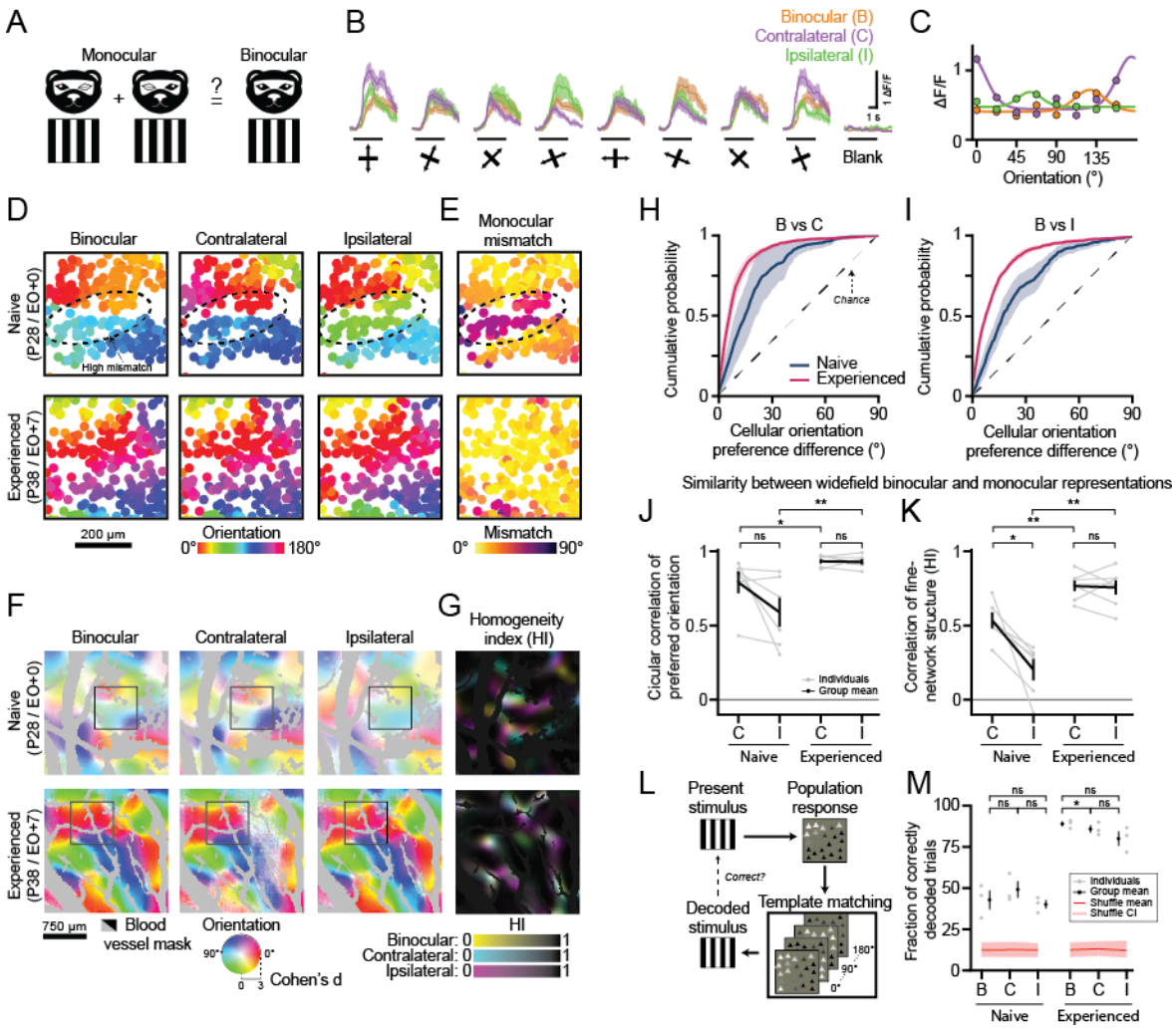


**Figure 4: Binocular stimulation yields a third orientation representation before eye-opening.**

**(A)** Schematic of experimental paradigm. **(B)** Representative cellular response traces (mean±SEM). The line under each response trace indicates visual stimulation period. **(C)** For cells in (B), the trial-average responses (median±MAD) and fit orientation tuning curves. **(D-E)** Representative cellular orientation preference maps (D) and monocular mismatch maps (E) for naive (top row) and experienced (bottom row) animals. Circles are cells and color represents either the preferred orientation or monocular mismatch. **(F-G)** Representative widefield maps of orientation preference (F) and homogeneity index maps (G) for naive (top row) and experienced (bottom row) animals. Preferred orientation and selectively (or homogeneity index) are respectively represented by image hue and saturation (or image color). Grayed or blacked out regions represent blood vessels, while boxed regions correspond to the cellular fields-of-view in (D-E). **(H-I)** Cumulative distributions of cellular orientation preference difference between the binocular and monocular preferred orientations (mean±SEM). **(J-K)** Circular correlation of the binocular to monocular

orientation preference maps (J) and Pearson's correlation of fine-network structure (homogeneity index) for the binocular to monocular preferred orientation maps (K) (mean±SEM). **(L)** Template-matching decoder schematic. **(M)** Fraction of correctly decoded trials to binocular and monocular stimulation (mean±SEM). Red line and shaded regions indicate the mean and 95% confidence intervals of decoding performance for shuffled data. Asterisks denote significance between groups (*:$p<0.05$,**:$p<0.01$, ns: $p>0.05$). Animal experiments: naive (n=3 cellular and n=6 widefield) and experienced (n=3 cellular and n=7 widefield).

(Supplementary Figure 3C, Pearson's correlation: Naive r=-0.25±0.12 vs Experienced r=-0.21±0.02 (Mean±SEM), n= 3 animals). Thus, we conclude that in naive animals monocular inputs constructively interact to generate a coherent representation of binocular orientation preference, even in cortical regions where monocular mismatch is high.

Next, we investigated whether early binocular responses reflect a distinct cortical representation or if they are related to one or more of the monocular representations. At the cellular-scale, the binocular preferred orientation of naive animals was not biased to either monocular preferred orientation (Figure 4H-I, Cellular orientation preference difference with binocular: Contralateral 19.12±6.83˚, Ipsilateral 23.40±4.29˚ (Mean±SEM), n=3 animals; Naive vs Experienced comparison: Binocular vs Contralateral p=0.104, Binocular vs Ipsilateral p=0.052, unpaired bootstrap test). We then tested whether the binocular response could be predicted base on the strength of the monocular responses, but the similarity of binocular and monocular preferred orientation was only weakly correlated to a cell's ocular dominance (Supplementary Figure 3D, Pearson's correlation with ODI in naive animals: Binocular vs Contralateral r=-0.20, $p<0.001$, Binocular vs Ipsilateral r=-0.20, $p<0.001$, n=3 animals). Our results therefore suggest that complex binocular interactions, including factors not reflected in suprathreshold responses, give rise to an orientation-specific binocular response that is distinct from the constituent monocular responses.

Consistent with our cellular-scale findings, at a network-scale preferred orientations of the binocular representation were not more correlated with the preferred orientation of either eye in naive animals, but did trend towards being more similar to the contralateral eye representation (Figure 4J, Circular correlation of preferred orientation with binocular in naive animals: Contralateral $r=0.79\pm0.05$, Ipsilateral $r=0.59\pm0.07$ (Mean±SEM), n=6 animals, $p=0.07$, paired permutation test). The fine topological features of the binocular representation in naive animals more closely matched the contralateral representation suggesting that synaptic drive from the contralateral eye may preferentially influence the complex binocular interactions underlying the binocular response (Figure 4K, Pearson's correlation of HI with binocular in naive animals: Contralateral $r=0.71\pm0.05$, Ipsilateral $r=0.46\pm0.07$ (Mean±SEM), n=6, $p=0.04$, paired permutation test). Nonetheless, the preferred orientation and network structure of the binocular representation became significantly better matched to the monocular representations after patterned visual experience (Figure 4J-K, Naive vs Experienced comparisons: Circular correlation of preferred orientation with binocular: Contralateral: $p=0.02$, Ipsilateral: $p<0.01$; Pearson's correlation of HI with binocular: Contralateral: $p=0.03$, Ipsilateral: $p<0.01$; n=6 vs 7 animals, unpaired permutation test). Together these results establish that the binocular representation of naive animals is not trivially related to either monocular representation and instead constitutes a third, distinct orientation representation.

Because three separate orientation representations emerge in the developing visual cortex prior to visual experience, we investigated if one of the representations was consistently further developed in encoding orientation-specific information at the cellular-scale. Here we employed a template matching decoder to predict the stimulus orientation presented on each trial by comparing trial-evoked population activity patterns to the best matching trial-averaged response pattern (Figure

4L)(Montijn et al., 2014). In naive animals, we could decode population responses from binocular and monocular stimulation at a rate higher than chance indicating that all three representations principally contribute to stimulus decoding (Figure 4M, Decoding performance in naive animals: Binocular 42.9±5.8%, Contralateral 49.5±5.0%, Ipsilateral 40.2±2.7% (Mean±SEM) vs chance 12.5%). Importantly, in naive animals, none of the orientation representations outperformed the others ($p>0.05$, paired bootstrap test), powerfully demonstrating that the binocular and monocular representations contain comparable decoding information about the stimulus orientation in naive animals.

**Shifts in cellular orientation preferences reduce monocular mismatch**

So far, we have demonstrated that three separate representations of orientation, two monocular and one binocular, emerge within the developing cortical circuitry before eye-opening, and that subsequent exposure to patterned visual experience drives functional reorganization towards a binocularly aligned representation. Early experience could drive alignment in binocularly responsive cells by inducing shifts in the preferred orientation for one or more of the orientation-specific representations. Alternatively, because we observed a continuum of mismatched cells, alignment could be achieved by driving the mismatched cells to become monocular, eliminating monocular mismatch and seeding the layout of ocular dominance columns. To investigate which of these mechanisms contributes to the alignment of the preferred orientation, in a cohort of animals we chronically tracked L2/3 neurons under two-photon imaging of GCaMP6s to monitor how the monocular and binocular orientation representations changed between eye-opening (naive) and four days after eye-opening (experienced) (Figure 5A-B, n=4 animals).

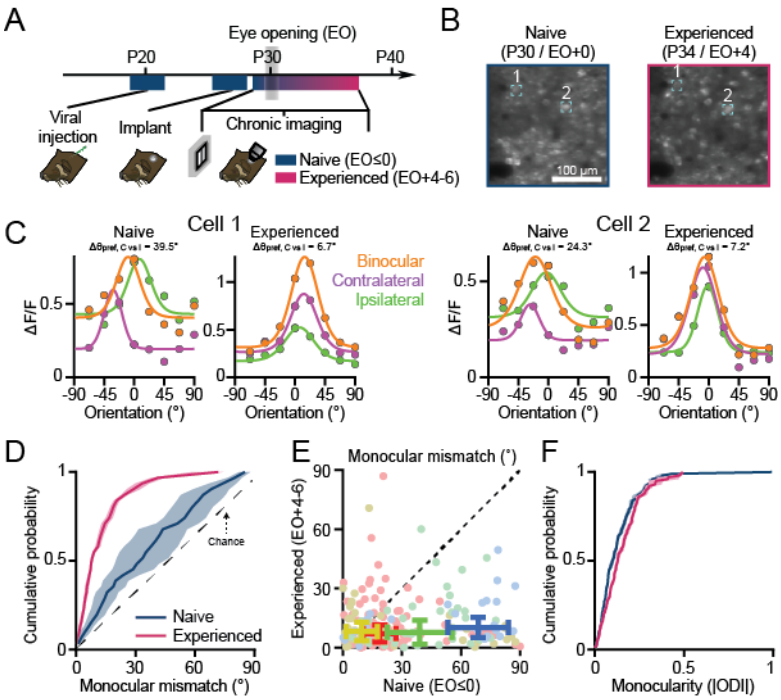


**Figure 5: Shifts in cellular orientation preferences reduce monocular mismatch.**

**(A)** Experimental timeline for chronic imaging. **(B)** An example field-of-view of chronically tracked cells before and after eye-opening. **(C)** The trial-average response (median±MAD) and fit orientation tuning curves for representative chronically tracked cells. **(D)** Cumulative distributions of monocular mismatch for chronically tracked cells before and after eye-opening (mean±SEM). **(E)** Scatter plot of the monocular mismatch for chronically tracked cells before and after eye-opening. The error bars represent the Median±MAD for each animal experiment (n=4 animals), while the color of each dot or error bar represents the animal experiment. **(F)** Cumulative distributions of monocularity (or |ODI|) for chronically tracked cells before and after eye-opening (mean±SEM).

Roughly half of the chronically tracked neurons displayed well-fit orientation tuned responses to binocular and monocular stimulation at eye-opening (39.13±3.29%, Mean±SEM). Neurons that maintained orientation selective responsiveness across imaging sessions (73.53±7.97%, Mean±SEM) displayed systematic reductions in preference mismatch across all three representations (Figure 5C-F, Supplementary Figure 4, Mean monocular mismatch: Naive

35.47±6.09˚ vs Experienced 12.73±0.94˚ (Mean±SEM), $p<0.001$, paired bootstrap test) suggesting that shifts in preferred orientation at the cellular-scale contribute to orientation alignment. Furthermore, the monocularity of binocularly responsive neurons modestly increased after four days of visual experience (Figure 5G, Monocularity: Naive 0.136±0.009 vs Experienced 0.154±0.003 (Mean±SEM), $p<0.05$, paired bootstrap test), including for the fraction of neurons that failed to maintain well-fit orientation selective responses after eye-opening (Monocularity: Naive 0.140±0.033 vs Experienced 0.247±0.09 (Mean±SEM), $p=0.38$, paired bootstrap test), and the degree of monocular mismatch at eye-opening did not predict the monocularity of individual neurons recorded days later (Bootstrapped Pearson's correlation: actual r=0.03 [-0.12, 0.17] vs surrogate r=0.14 [-0.02, 0.30], Median [CI]). These results suggest that orientation alignment is primarily driven by systematic reorganization of the preferred orientation within the first four days of patterned visual experience, and that neurons likely become more monocular after the preferred orientation is matched (as previously shown in Figure 1H-I).

**Early orientation representations reorganize to a unified representation resembling the early binocular representation.**

We next investigated if cellular-scale activity patterns at eye-opening are related to the binocularly unified representation that becomes evident days later. Using a template matching decoder based on the trial-averaged response of the experienced monocular and binocular responses, we decoded the presented stimulus orientation at rates above chance levels for trial-evoked population responses recorded at eye-opening (Supplementary Figure 5A-C, Fraction of correctly decoded trials: Binocular 21.5±3.1%, Contralateral 17.92±2.0%, Ipsilateral 20.82±2.4% (Mean±SEM) vs Shuffles 12.5% [8.13, 16.88], Mean [CI]). Nonetheless, decoding accuracy based on the trial-

averaged response of the experienced representations was substantially worse than with trial-average responses at eye-opening ($p<0.001$ for all comparisons, paired bootstrap test). Our results suggest that at the cellular-scale, the binocularly aligned responses of experienced animals coarsely resemble population responses produced earlier at eye-opening.

Similarity between population responses evoked before and after eye-opening raises the possibility that the binocularly unified representation after eye-opening could be related to one or more of the naive representations present at eye-opening. While our relatively restricted two-photon calcium imaging fields (~700μm) obscured differences in the stability of the monocular and binocular representations (Supplementary Figure 5D-G, Mean orientation preference difference: Binocular 31.14±4.12˚, Contralateral 30.06±4.06˚, Ipsilateral 30.13±4.78˚ (Mean±SEM), $p>0.05$ for all comparisons, paired bootstrap test), coverage in the range of preferred orientations represented by the binocular representation was higher than for the monocular representations at eye-opening (Supplementary Figure 5H, Normalized difference from a uniform distribution: Binocular 0.51±0.05, Contralateral 0.65±0.02, Ipsilateral 0.66±0.03 (Mean±SEM); Binocular vs Contralateral: $p=0.03$, Binocular vs Ipsilateral: $p=0.001$, Contralateral vs Ipsilateral: $p>0.05$). These results raise the possibility that orientation hypercolumns are larger for the monocular representations than the binocular representation at eye-opening.

To investigate this possibility, we turned to chronic widefield imaging (n=12 animals, Supplementary Figure 6A), confirmed that the three representations were aligned following experience, and then used an established wavelet method to measure the width of orientation hypercolumns chronically (Supplementary Figure 6C,E-H)(Kaschube et al., 2010). Orientation hypercolumns at eye-opening were larger for the monocular representations than the binocular representation (Supplementary Figure 6D, Orientation hypercolumn wavelength for Naive:

Binocular 876.2±45.4μm, Contralateral 1021.7±54.2μm, Ipsilateral 1097.9±65.1μm (Mean±SEM); Binocular vs Contralateral: $p<0.001$, Binocular vs Ipsilateral: $p=0.02$, Contralateral vs Ipsilateral: $p>0.05$, paired bootstrap test). Furthermore, by accounting for brain-related growth using landmark-based image registration, we found that orientation hypercolumns were smaller after eye-opening (Supplementary Figure 6D, Orientation hypercolumn wavelength for Experienced: Binocular 767.9±27.2μm, Contralateral 815.2±37.4μm, Ipsilateral 861.4±39.3μm (Mean±SEM); Naive vs Experienced: $p<0.001$ for all comparisons, paired bootstrap test), but the relative change in the binocular representation (~12%) was more modest compared to the monocular representations (~20%).

Smaller changes in orientation hypercolumn width for the binocular representation suggest that the binocular representation could be more stable than the monocular representations (Figure 6C). Consistent with this hypothesis, we discovered that the layout of the preferred orientation for the binocular representation was significantly more stable than either of the monocular representations (Figure 6A,D, Circular correlation of the preferred orientation: Binocular $r=0.40\pm0.04$, Contralateral $r=0.30\pm0.04$, Ipsilateral $r=0.16\pm0.04$ (Mean±SEM), $n=12$ animals; Binocular vs Contralateral: $p=0.02$, Binocular vs Ipsilateral: $p<0.01$, Contralateral vs Ipsilateral: $p=0.06$, paired permutation test). If the binocular representation is more stable than the monocular representations, the fine-network structure of the binocular representation should remain more stable than the monocular representations. Indeed, as assessed by HI, the fine-network structure of the binocular representation changes less than the monocular representations (Figure 6B,E, Pearson's correlation of HI: Binocular $r=0.40\pm0.06$, Contralateral $r=0.26\pm0.04$, Ipsilateral $r=0.12\pm0.07$ (Mean±SEM); Binocular vs Contralateral: $p=0.01$, Binocular vs Ipsilateral: $p<0.01$, Contralateral vs Ipsilateral $p=0.10$, paired bootstrap test). These results demonstrate that the naive binocular representation is

more stable than the monocular representations and suggests that the naive binocular representation might more closely resemble the binocularly unified representation after eye-opening.

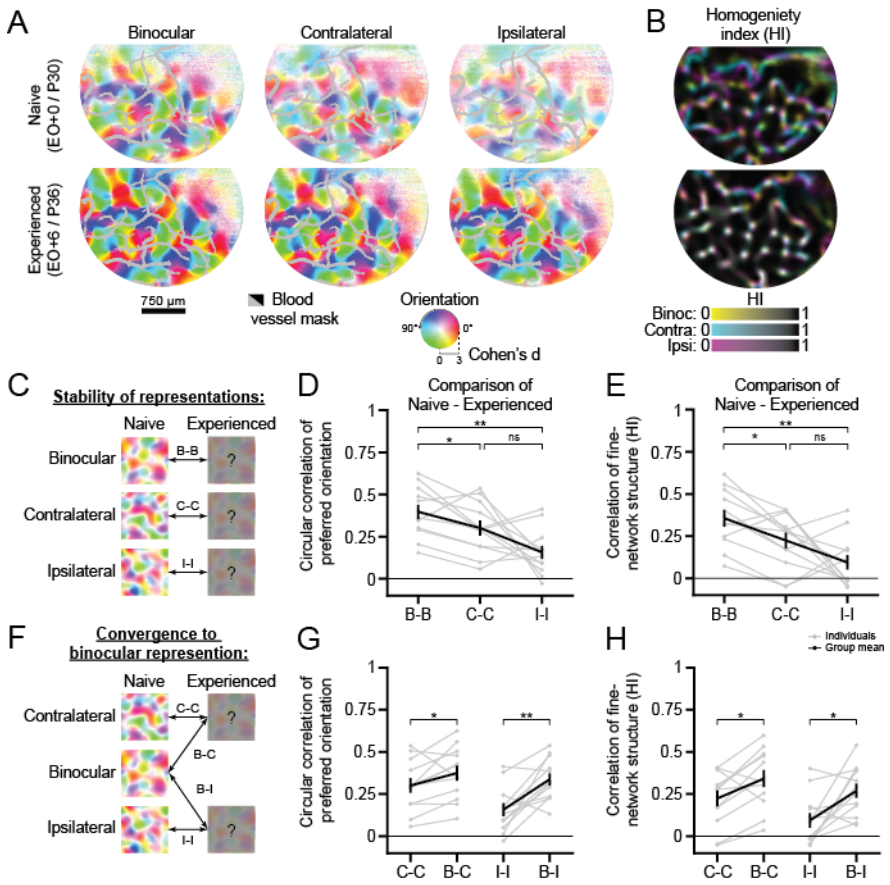


**Figure 6: Early orientation representations reorganize to a unified representation resembling the early binocular representation.**

**(A-B)** Representative widefield maps of orientation preference (A) and homogeneity index maps (B) before and after eye-opening from a chronically imaged animal (top and bottom rows respectively). Preferred orientation and orientation selectively (or homogeneity index) are respectively represented by image hue and saturation (or image color). Grayed or blacked out regions represent blood vessels. **(C)** Schematic for determining the stability of the monocular and binocular representations before and after eye-opening. **(D-E)** Circular correlation of the preferred orientation (D) and Pearson's correlation of fine-network structure (homogeneity index) (E) for comparing the stability of the binocular and monocular orientation preference maps before and after eye-opening (mean±SEM). **(F)** Schematic

for determining if the experienced monocular orientation preference maps are more similar to the naive binocular or naive monocular orientation preference maps. **(G-H)** Circular correlation of the preferred orientation (G) and Pearson's correlation of fine-network structure (homogeneity index) (H) for comparing the experienced monocular orientation preference maps either to the naive binocular or naive monocular orientation preference maps (mean±SEM). Gray and black lines/dots in (D-E, G-H) reflect either individual or grouped measurements (n=12 animals), while asterisks denote significance between groups (*:$p<0.05$,**:$p<0.01$, ns: $p>0.05$).

To directly test this hypothesis, we examined whether each experienced monocular representation more closely matched the naive binocular representation at eye-opening than the corresponding naive monocular representation (Figure 6F). Indeed, we found that both the layout of preferred orientation and fine-network structure for the naive binocular representation better predicted the experienced monocular representations (Figure 6G-H, Circular correlation of the preferred orientation: Experienced contralateral vs Naive contralateral r=0.30±0.04 or Naive binocular r=0.38±0.05, p=0.048, Experienced ipsilateral vs Naive ipsilateral r=0.16±0.04 or Naive binocular r=0.34±0.04, p<0.01; Pearson's correlation of HI: Experienced contralateral vs Naive contralateral r=0.22±0.05 or Naive binocular r=0.34±0.05, p=0.02, Experienced ipsilateral vs Naive ipsilateral r=0.16±0.04 or Naive binocular r=0.34±0.05, p=0.02, paired bootstrap test). Taken together with deprivation experiments, our results suggest that the naive binocular representation anchors orientation tuning in the developing primary visual cortex, and that the heightened stability of the binocular representation likely arises from the shared visual experience of the eyes after eye-opening.

## Discussion

Our results provide novel insights into the process that underlies the development of a unified binocular representation of orientation preference in primary visual cortex. Contrary to the prevailing view that the preferred orientation is stable across early development (Chapman et al., 1996; Godecke and Bonhoeffer, 1996; Sengpiel et al., 1998; Wiesel and Hubel, 1974), our study demonstrates substantial reorganization in the preferred orientation, changes evident at the cellular-scale and network-scale that are critical for aligning the orientation representations. Using two-photon and widefield calcium imaging, we demonstrate for the first time that there are three distinct representations of orientation by eye-opening: one representation for each eye, and a third representation revealed by binocular stimulation. We then demonstrate that subsequent binocular experience is necessary to drive network-scale alignment of these distinct orientation representations towards a binocularly unified representation. The alignment process we report here in an animal with columnar architecture is consistent and expands upon the single-cell matching process recently reported in the developing mouse (Gu and Cang, 2016; Wang et al., 2010; Yaeger et al., 2019), suggesting that many aspects to the development of orientation preference are conserved across species. While our observations conflict with a previous study in young kittens, which concluded that matched monocular representations sequentially develop (Crair et al., 1998), multiple factors may contribute to the different conclusions reached, such as species differences or reliance on intrinsic signal imaging, a less-sensitive technique for assessing the preferred orientation. Regardless, our results show that an experience-dependent process in a cortex with a columnar architecture is capable of reorganizing the early representations of stimulus orientation into a mature, binocularly unified representation.

Importantly, our study extends upon previous single-cell electrophysiology studies in rodents by demonstrating that early orientation preference differences in individual neurons reflect systematic misalignment of the network-scale representations of preferred orientation. Recent studies in developing mice suggest that neurons sharing similar orientation preferences form preferentially connected microcircuits only after eye-opening (Ko et al., 2013; Ko et al., 2014). Because feature-specific connectivity is largely absent in visually naive mice, orientation preference differences could feasibly arise from neurons independently selecting feedforward inputs from each eye and acquiring orientation preference differences on a per-cell basis. Yet our population imaging data in ferrets offers a different account for how early orientation preference differences in neurons manifests as network-scale misalignment of the monocular and binocular orientation representations. Orientation-specific microcircuits must already be coarsely established by eye-opening for separate orientation-specific representations to emerge for each eye. In support of this view, chronic imaging in the developing ferret shows that the correlation structure of spontaneous activity patterns before eye-opening predicts the layout of the preferred orientation that becomes evident after eye-opening suggesting that early microcircuits develop without patterned visual experience (Smith et al., 2018). Thus, we conclude that early monocular mismatches reflect the emergence of misaligned monocular network representations, and that early experience is necessary to drive network-scale alignment of these emerging representations.

A surprising aspect to early alignment of orientation representations is that this developmental process occurs during a critical time window when neural responses are tremendously binocular. The critical period of ocular dominance plasticity begins in ferrets about one week after eye-opening (Issa et al., 1999), suggesting that early binocular alignment of orientation representations during the first week of visual experience precedes the normal critical-period for ocular dominance

plasticity. Consistent with this hypothesis, we did not observe a dependence of the monocular matching process on the monocularity of cells. Furthermore, our deprivation experiments indicate that alignment of the preferred orientation is impaired in animals where patterned visual experience is delayed by one-week. These results contrast to recent chronic calcium imaging experiments in environmentally-enriched mice, where rescue of the monocular matching process in monocularly deprived animals depends on ocular dominance (Levine et al., 2017). Similarly, reverse-lid suture experiments in young kittens demonstrate that binocularly correlated visual input is unnecessary to develop matched monocular representations of orientation (Godecke and Bonhoeffer, 1996). Together these studies suggest that alignment of the preferred orientation in animals recovering from monocular deprivation, during a later developmental stage where cells are strongly monocular, benefits from the establishment of the orientation representation by the dominant eye. In contrast, monocular inputs cooperatively interact across normal development to align the preferred orientation in an experience-dependent manner during the first week of visual experience.

While previous studies have focused on the competition of monocular inputs in the development of ocular dominance (Bienenstock et al., 1982; Blakemore and Van Sluyters, 1974; Katz and Shatz, 1996; Miller et al., 1989; Trachtenberg, 2015), our findings highlight the cooperative nature of ocular interactions in the generation of orientation representations and the importance of examining both binocular and monocular responses. Our deprivation experiments clearly show that patterned binocular visual experience is important for the alignment of the orientation representations, as well as the maintenance of spatially-clustered responses. This is consistent with growing evidence that binocular visual experience both during and after the critical period of visual development can improve visual acuity and correct deficits associated with amblyopia (Birch et

al., 2015; Hess et al., 2010; Murphy et al., 2015). Thus, shared sensory experience by the eyes appears crucial for the proper maturation of binocular interactions and the normal development of visual responses.

The development of orientation selectivity and ocular dominance in primary visual cortex has long been an area of active interest for theoretical modeling efforts to understand the emergence of structured representations in the brain (Bednar and Miikkulainen, 2006; Durbin and Mitchison, 1990; Kohonen, 1988; Koulakov and Chklovskii, 2001; Miller, 1994; Stevens et al., 2013; von der Malsburg, 1973; Wolf, 2005), including a unified binocular representation of orientation (Bhaumik and Shah, 2014; Erwin and Miller, 1998; Shouval et al., 2000; Wolf et al., 1996). In previous studies it has been suggested that specific interocular correlations that arise from natural binocular experience play a role in the co-emergence of ocular dominance and matched orientation preferences (Erwin and Miller, 1998). Instead our study highlights that the emergence of monocular orientation tuning in visual cortex is nearly independent at the onset of visual experience, and is consistent with many theoretical frameworks of self-organization, which predict substantial functional reorganization as the dynamical system develops towards a stable configuration (Goodhill, 2007). Yet our results surprisingly highlight that the early monocular representations undergo more functional reorganization than the binocular representation, which has not been predicted by previous modeling efforts. Thus, we suggest that in order to fully appreciate the dynamics involved in the emergence of orientation-specific representations, it is necessary to understand the relationship between monocular and binocular responses.

To the best of our knowledge, our study is the first to chronically track the cellular changes underlying the normal alignment of sensory representations. At a cellular level, we show that chronically tracked cells display shifts in preferred orientation reflecting reorganization of the

orientation representations, rather than systematic loss of responsiveness to monocular input for one of the eyes in mismatched cells that could have accounted for the organization of ocular dominance. Furthermore, across the neural population, our widefield epifluorescence imaging data demonstrates that the monocular representations undergo substantially more reorganization than the binocular representation. These results suggest that concordant binocular vision after eye-opening instructs the development of a unified orientation representation. This conclusion contrasts with the prevailing views for alignment of sensory representations, which focus on either the experience-independent development of matched sensory representations or the experience-dependent alignment of one sensory representation to another (Cang and Feldheim, 2013; Cang et al., 2005; Chandrasekaran et al., 2005; Hyde and Knudsen, 2001; Knudsen and Knudsen, 1989; Smith and Trachtenberg, 2007; Triplett et al., 2009). Thus, our data suggests a novel, third solution to sensory representation alignment, where constructive interactions between segregated inputs lead to a novel representation, which through experience serves as a template for aligning the constituent representations into a single unified representation. In conclusion, our findings suggest that the constructive interaction of monocular inputs builds a binocular representation of orientation tuning that instructs the alignment of the monocular representations through an experience-dependent learning process.

## Methods

**Animals.** All experimental procedures were approved by the Max Planck Florida Institute for Neuroscience Institutional Animal Care and Use committee and were performed in accordance with guidelines from the U.S. National Institute of Health. Juvenile female ferrets from Marshal Farms were co-housed with jills on a 16-h light/8-h dark cycle.

**Viral injections.** Viral injections were performed as previously described(Smith et al., 2018). Briefly we expressed GCaMP6s by microinjection of AAV2/1-hSyn-GCaMP6s-WPRE-SV40 (University of Pennsylvania Vector Core) into the visual cortex 6-14 days before imaging experiments. Anesthesia induction was performed using either ketamine (50mg/kg, IM) and/or isoflurane (1-3%) delivered in $O_2$ and then maintained with isofluorane (1-2%). Atropine (0.2mg/kg, IM) was administered to reduce secretions, while Buprenorphine (0.01mg/kg, IM) and a 1:1 mixture of lidocaine and bupivacaine (injected directly into the scalp) were administered as analgesics. Animal temperatures were maintained at 37°C using a homeothermic heating blanket. Animals were also mechanically ventilated and both heart rate and end-tidal CO2 were monitored throughout the surgery. Under aseptic surgical technique, a small craniotomy was made over visual cortex 6.5-7 mm lateral and 2mm anterior to lambda. Approximately 1µL of virus was pressure infused into the cortex through a pulled glass pipette across two depths (~200µm and 400µm below the surface). This procedure reliably produced robust and widespread GCaMP6s expression in excitatory neurons over an area >3 mm in diameter (Smith et al., 2018). To improve the uniformity of the GCaMP6s expression, sometimes an additional injection of 1µL of virus was pressure injected into a separate region of cortex displaced ~1-1.5mm away from the first injection site.

**Eyelid Suture Procedure.** In deprivation and chronic imaging experiments, eyelids were binocularly sutured during a short surgical procedure between P26-P30. Anesthesia was induced

with isoflurane (2-5%) and Buprenorphine (0.01mg/kg, IM) was administered. Using aseptic technique, both eyelids were sutured shut using continuous sutures (6-0 Ethilon suture). During recovery, antibiotic ointment was applied to the suture eyelid margins. Eyelid sutures were monitored daily until removed during an imaging experiment as noted in the main text.

**Cranial window surgery.** Animals were anesthetized and prepared for surgery as described above. In acute imaging experiments, skin and muscle overlying visual cortex were reflected and a custom-designed metal headplate (8mm DIA) was implanted over the injected region with MetaBond (Parkell Inc.). Then a craniotomy (~5mm) and a subsequent durotomy were performed, and the underlying brain stabilized with a custom-designed titanium metal cannula (4.5mm DIA, 1.5mm height) adhered to a thin 4mm coverslip (Warner Instruments) with optical glue (#71, Norland Products, Inc). The headplate was hermetically sealed with a stainless-steel retaining ring (5/16" internal retaining ring, McMaster-Carr) and glue (VetBond, 3M or Krazy Glue).

To allow repeated access to the same imaging field in chronic imaging experiments, cranial windows were implanted in each animal 2 days prior to the first imaging session. Using aseptic surgical technique, skin and muscle overlying the dorsal brain surface were gently reflected. To reduce the chances of an implant failure for our cranial window, we used a two-piece design. We adhered a metal headpost (7x7mm) to the skull ~3.5mm anterior of bregma and a separate custom-designed, chamber implant overlying the injected region using MetaBond and black dental acrylic. Like the acute experiments, we performed a similar craniotomy, durotomy, and inserted the same custom-designed titanium metal cannula. At the end of the survival cranial window implant surgery, the metal cannula was sealed with a silicone polymer plug (Kwik-kast, World Precision Instruments) to protect the imaging window between imaging experiments.

**Calcium Imaging Experiments.** Widefield epifluoresence imaging of GCaMP6s was achieved with a Zyla 5.5 sCMOS camera (Andor) controlled by µManager (Edelstein et al., 2010). Images were acquired at 15Hz with 4x4 binning to yield 640x540 pixels through a 4x air-immersion objective (Olympus, UPlanFL 4x N/0.13NA). For analysis, images were spatially downsampled by a factor of 2x to yield 320x270 pixels at a spatial resolution of 11.63µm/pixel. Two-photon imaging of GCaMP6s was performed with a B-Scope microscope (ThorLabs) driven by a Mai-Tai DeepSee laser (Spectra Physics) at 940nm. The B-Scope microscope was controlled by ScanImage (Vidreo Technologies) in a resonant-galvo configuration with multi-plane images (512x512 pixels) being sequentially collected across either one or four imaging planes using a piezoelectric actuator for an effective frame rate of 30Hz or 6Hz respectively. Images were acquired at 2x zoom through a 16x water immersion objective (Nikon, LWD 16X W/0.80NA) yielding cellular fields-of-views of ~0.7mm on each side (1.36µm/pixel).

Imaging experiments fell into two broad categories: acute and survival imaging experiments. Acute imaging experiments began immediately after the cranial window surgery. For survival imaging experiments, where animals had a cranial window implanted days earlier, anesthesia was induced with isoflurane (2-5%) and atropine (0.2mg/kg) was administered. Animals were intubated and ventilated, and an IV catheter was placed in the cephalic vein. The silicon polymer plug overlying the sealed imaging chamber was gently peeled off. Whenever the imaging quality of the chronic cranial window was found to be suboptimal for imaging, the chamber was opened under aseptic conditions, any regrown tissue/neomembrane was removed, and a new coverslip was inserted.

For both acute and survival imaging experiments, eyelid sutures were removed or eyelids were separated where applicable to ensure visual stimulation was always presented to open eyes.

Phenylephrine (1.25-5%) and tropicamide (0.5%) were applied to the eyes to retract the nictitating membrane and dilate the pupil, and the cornea was protected with regular application of eye drops (Systane Ultra, Alcon Laboratories). Prior to imaging, isoflurane levels were reduced from a surgical plane to ~1-1.5%. After reaching a stable, anesthetic baseline for 30 minutes (~280-300bpm), animals were paralyzed with pancuronium bromide (0.1 mg/kg/hr in lactated Ringer's with 5% dextrose, delivered IV). Upon completion of imaging in acute experiments, isoflurane was raised to 5% and given Euthasol (0.5ml, IV). In survival experiments, animals were instead recovered from anesthesia and returned to their home cages. During recovery, up to 3 repeated doses of neostigmine (0.06mg/kg/hr, IV) and atropine (0.05mg/kg/hr, IV) were used to reverse paralysis.

**Visual stimulation.** Visual stimuli were delivered on a LCD screen placed approximately 25–30cm in front of the eyes using PsychoPy (Peirce, 2007). To evoke orientation responses, full-field square gratings at 100% contrast, at 0.015 or 0.06 cycles per degree and drifting at 1 or 4 Hz were presented at 8 or16 directions. In addition, “blank” stimuli of 0% contrast were also presented. Stimuli were randomly interleaved and presented for 3-4s followed by 3-6s of gray screen.

**General Analysis.** All data analysis was performed using custom written scripts in either Python, Matlab, or ImageJ. Early pre-processing steps for analysis were common to both two-photon and widefield epifluorescence imaging data. First, to correct for brain movement during imaging, we registered every imaging frame by maximizing phase correlation to a common reference frame. Furthermore, every imaging experiment acquired during a single day were registered into one reference frame. ROI segmentation was performed manually in widefield epifluorescence imaging by manually drawing around cortical regions with robust visually evoked activity, while cellular ROIs were drawn using custom software in ImageJ (Cell Magic Wand)(Wilson et al., 2017). The

raw fluorescence trace for each cellular trace was the average fluorescence trace across all pixels within the ROI. The baseline $F_0$ for each pixel/cell was obtained by applying a rank-order filter to the raw fluorescence trace (25-30$^{th}$ percentile) with a time window of 60s. The baseline corrected evoked activity was calculated as $(F-F_0)/F_0 = \Delta F/F_0$. Grating evoked responses were then calculated as the difference of the average of the fluorescence $\Delta F/F_0$ over the full stimulus period (3-4s) and the average of the fluorescence $\Delta F/F_0$ over the pre-stimulus period (1.5-2s). Trial-averaged responses were calculated by taking the median across repeated trials to the same stimulus orientation.

**Widefield Epifluorescence Imaging.** For analysis of the wide-field epifluorescence imaging data, spatial filtering was necessary to eliminate signal strength variations and measurement noise. To determine an appropriate high-pass filter cutoff that did not fundamentally alter the underlying modular response, we first computed the average size (i.e. wavelength) of orientation hypercolumns for each imaging experiment using an established wavelet technique (Kaschube et al., 2010). First, we computed a spatially unfiltered orientation preference map using the vector-sum approach:

$$z(x) = \sum_{\theta=0^\circ}^{180^\circ} R(x,\theta) * e^{i*2\pi*\theta/180^\circ}$$

, where z(x) is the complex-field orientation response and R(x,θ) is the trial-averaged response to an oriented, drifting grating (θ) at each pixel (x). We then independently fit an array of wavelet coefficients, $\hat{I}(x,\theta,l)$ to the z-scored real- and imaginary- components of z(x):

$$\hat{I}(x,\theta,l) = \int_{ROI} \left( Image(y)\, l^{-1}\ \psi_{x,\theta,l}\left(\Omega^{-1}(\theta)\frac{y-x}{l}, l\right)\right) d^2y$$

$$\psi(\boldsymbol{r}, l) = \exp\left(i\mathrm{k}_{\varphi}(l)r - \frac{1}{2}\left(r_1^2 + \frac{r_2^2}{\sigma^2}\right)\right)$$

$$\Omega(\theta) = \begin{pmatrix} cos\theta & -sin\theta \\ sin\theta & cos\theta \end{pmatrix}$$

where $\psi_{x,\theta,l}$ is the complex Morlet wavelet, Ω(θ) is the 2D rotation matrix, (x, θ, $l$) are the position, orientation, and scale of the wavelet, and $\mathrm{k}_{\varphi}$ and σ are the characteristic wavenumber and anisotropy of the wavelet. Relatively small, isotropic wavelets ($\mathbf{k}_{\boldsymbol{\varphi}}$= (2,0) and σ=1) were used to measure the local size or wavelength of orientation hypercolumns . Each wavelet's orientation (θ) was rotated between 16 uniformly spaced orientations. The wavelet's scale (l) was varied between a range of [0.4 1.8] mm with a step size of 0.05 mm. The wavelet domain spacing, Λ(x), was computed with the following formulas:

$$l(x) = \arg\max_l \left(\sum_{\theta=0^\circ}^{180^\circ} \hat{I}(\boldsymbol{x}, \theta, l)\right)$$

$$\Lambda(x) = l(x)\left(\frac{2\pi}{k_{\varphi}}\right)$$

where x is the pixel location and $l(x)$ corresponds to the scale of the wavelet that maximized the angle averaged array of wavelet coefficients (using cubic splines interpolation). The wavelength of orientation hypercolumns, $\overline{\Lambda(ROI)}$, for each animal experiment was then defined as the mean wavelet domain spacing over the entire ROI and across both fits to the z-scored real- and imaginary- components of z(x). For quantification of the wavelength in Supplementary Figure 6, the wavelength was computed again, but instead on the vector sum of the $Cohen's\ d\ (\theta, x)$ spatially filtered, single-condition maps (see below).

We spatially filtered each trial-evoked response image using a spatial bandpass filter, where the low-pass filter cutoff was defined as 50μm and the high-pass filter cutoff was defined as the mean orientation hypercolumn wavelength across monocular and binocular stimulation. A spatial filter was applied to each image in the Fourier Domain, using a filter kernel based on the Fermi-Dirac distribution:

$$Filtered\ Image(x) = \mathcal{F}^{-1}\left(\mathcal{F}[Image(x)] * Filter\left(k_{lp}, k\right) * \left[1 - Filter\left(k_{hp}, k\right)\right]\right)$$

$$Filter\left(k_{cutoff}, k\right) = \frac{1}{1 + e^{\frac{|k| - k_{cutoff}}{\beta * k_{cutoff}}}}$$

where $\mathcal{F}$ denotes the forward Fourier transform, $\mathcal{F}^{-1}$ denotes the inverse Fourier transform, k is the spatial wave-number ($k = 2\pi/\lambda$), $k_{cutoff}$ is the filter cutoff (low-pass cutoff ($l_{lp}$): 2π/0.25mm, high-pass cutoff ($l_{hp}$): 2π/1.6mm), and β is the steepness parameter of the fermi-filter (T = 0.05). To maintain the original response amplitude of the population responses, spatially filtered images were ranged-fitted, such that the 5$^{th}$ and 95$^{th}$ percentiles intensity values matched the original, unfiltered images.

To evaluate orientation selective responses, we computed normalized single-condition response maps using the Cohen's d metric, rather than the customary OSI or 1-CV metrics, to account for response variance across trials:

$$Cohen's\ d\ (\theta, x) = \frac{\mu\ (x, \theta) - \mu\ (x)}{\sqrt{\frac{(n_{trials} - 1)\ \sigma(x, \theta)^2 - (n_\theta * n_{trials} - 1)\ \sigma(x)^2}{(n_\theta + 1) * n_{trials} - 2}}}$$

$$\mu(\theta, x) = \sum_{i=1}^{n_{trials}} R_i\ (x, \theta)/n_{trials}$$

$$\mu(x) = \sum_{\theta=0^\circ}^{180^\circ} \mu\ (x, \theta)/n_\theta$$

$$\sigma(\theta, x) = \sqrt{\sum_{i=1}^{n_{trials}} (R_i(x,\theta) - \mu\,(x,\theta))^2/(n_{trials} - 1)}$$

$$\sigma(x) = \sqrt{\sum_{\theta=0°}^{180°} \sum_{i=1}^{n_{trials}} (R_i(x,\theta) - \mu\,(x))^2/(n_\theta * n_{trials} - 1)}$$

where $n_{trials}$ is the number of trials, and $n_\theta$ is the number of stimulus conditions, and $R_i(x,\theta)$ is the evoked response to an oriented, drifting grating ($\theta$) for trial $i$ at pixel ($\theta$). Preferred orientation ($\theta_{pref(x)}$, ranging from 0 to 180°) and orientation selectivity (r) was computed as the vector sum of the $Cohen's\ d\ (\theta, x)$ single-condition maps:

$$z(x) = \sum_{\theta=0°}^{360°} Cohen's\ d\ (\theta, x) * \ e^{i*2\pi*\theta/180°}$$

$$\theta_{pref}(x) = \arg\big(z(x)\big) = \tan^{-1}\frac{real\big(z(x)\big)}{imag\big(z(x)\big)}$$

$$r = |z| = \sqrt{real\big(z(x)\big)^2 + imag\big(z(x)\big)^2}$$

For each pixel, a permutation test (n=100) was used to evaluate if orientation selectivity was significant (p>0.05). Pixels were considered well-tuned if they exhibited statistically significant orientation selectivity for both monocular and binocular stimulation. We excluded any pixels overlying blood-vessels that could be observed in the raw fluorescence images. Monocular

mismatch was computed as the absolute angular difference between the contralateral and ipsilateral preferred orientations:

$$Monocular\ mismatch(x) = \left|\theta_{contra}(x) - \theta_{ipsi}(x)\right| = \left(\frac{180°}{2\pi}\right)\left|\arg\left(\frac{e^{i*2\pi*\theta_{contra}/180°}}{e^{i*2\pi*\theta_{ipsi}/180°}}\right)\right|$$

where $\theta_{contra}$and $\theta_{ipsi}$ are the preferred orientations for each eye at pixel $(x)$. To ensure that the measured monocular mismatch for the population could not be artifactually explained by high variation in the preferred orientation, we evaluated the worst-case measurement error. Here we bootstrap resampled trial-averaged responses using replacement and recomputed the preferred orientation (n=1,000). The measurement error for each pixel was defined as the median error of the bootstrapped preferred orientations with the measured preferred orientation. We then defined our worst case measurement error as the value of the pixel exhibiting large measurement error (95$^{th}$ percentile).

Orientation preference differences between the monocular and binocular preferred orientations were computed using a similar formula to the monocular mismatch, but switching the preferred orientations of the comparisons. The circular correlation was used to assess differences in the layout of preferred orientation for monocular and binocular orientation maps:

$$r = \frac{4a(x)b(x)}{\sqrt{c(x)d(x)}}$$

$$a(x) = \sum \cos\theta_{contra}(x)\cos\theta_{ipsi}(x) * \sum \sin\theta_{contra}(x)\sin\theta_{ipsi}(x)$$

$$b(x) = \sum \cos\theta_{contra}(x)\sin\theta_{ipsi}(x) * \sum \sin\theta_{contra}(x)\cos\theta_{ipsi}(x)$$

$$c(x) = n^2 - \sum \cos 2\theta_{contra}(x)^2 - \sum \sin 2\theta_{contra}(x)^2$$

$$d(x) = n^2 - \sum \cos 2\theta_{ipsi}(x)^2 - \sum \sin 2\theta_{ipsi}(x)^2$$

where $r$ is the circular correlation, $x$ is the index of pixels, and $n$ is the number of all orientation selective pixels. For computing the similarity of the fine network structure in orientation preference maps, we computed the Homogeneity Index (Wilson et al., 2017):

$$HI(x) = \left| \frac{\sum_{k=1}^{n} e^{-2i\pi\theta_k}}{n} \right|$$

where $n$ is the number of pixels within 100 μm of the seed pixel ($x$) and $\theta_k$ is the preference of the $k^{th}$ pixel in the sample. We then quantified the similarity between the Homogeneity Index maps for the monocular and binocular orientation maps using Pearson's correlation.

**Two-Photon Imaging**

Cells were considered responsive if the trial-averaged response to any stimulus orientation for either monocular or binocular stimulation was greater than two standard deviations of the response to a blank stimulus. The preferred orientation for responsive cells was assessed by fitting a Von Mises function to the trial-averaged responses:

$$R\ (\theta) = \frac{e^{\kappa \cos(\theta - \theta_{pref})}}{2\pi\ I_0(\kappa)}$$

where $R\ (\theta)$ is the trial-averaged response, $\theta$ is the stimulation orientation, $\theta_{pref}$ is the preferred orientation, $\kappa$ controls the orientation width, and $I_0(\kappa)$ is a zero-order Bessel function. Cells were considered well-tuned if the $R^2$ value of the orientation fits to monocular and binocular stimulation were all ≥0.5. To evaluate a cell's orientation selectivity, we used the Cohen's d metric and compared the responses of the preferred and orthogonal orientations. Spatial clustering of the preferred orientation or monocular mismatch was assessed by calculating the

pairwise correlation for cells located within a fixed range from each other, ranging from distances of 50 µm to 500 µm. To evaluate the degree that all preferred orientations are represented uniformly within each of our cellular fields, we estimated the normalized difference from a uniform distribution using the following metric:

$$Normalized\ difference = \sum_{i=1}^{n} \frac{|Histogram(i) - 1|}{2n}$$

where $n$ is the number of cells, $Histogram(i)$ is the indexed histogram of preferred orientations, ranging from 0˚ to 180˚ with a bin size equal to $n$, $i$ is the index for the histogram bins. The normalized difference metric ranges from 0 (all orientations equally represented) to 1 (only a single representation represented). Monocular mismatch, orientation preference differences, measurement error, and the homogeneity index were computed using the same formulas previously described used for pixels (*see widefield imaging section*).

To evaluate the degree that monocular input from one eye consistently drove stronger responses, we computed the ocular dominance index (ODI):

$$ODI = \frac{\sum_{\theta=0^\circ}^{180^\circ} \left(R_{contra}(\theta) - R_{ipsi}(\theta)\right)}{\sum_{\theta=0^\circ}^{180^\circ} \left(R_{contra}(\theta) + R_{ipsi}(\theta)\right)}$$

where $R_{contra}(\theta)$ and $R_{ipsi}(\theta)$ are the trial-averaged responses to contralateral and ipsilateral stimulation and θ is the stimulation orientation. ODI values range from -1 to +1, where 0 indicates a lack of bias and -1 and +1 values indicate complete dominance from either the ipsilateral or contralateral eyes respectively. Monocularity was defined as the magnitude of the ODI, with values ranging from +0 (binocular) to +1 (monocular).

To decode the stimulus orientation from the population activity vectors recorded during each trial, we used a normalized template matching algorithm (Montijn et al., 2014). In an effort to evaluate the decoding based on the relative responsiveness of each cell, the trial evoked $\Delta F/F_0$ responses of each cell were first individually z-scored:

$$Z(\theta, \mathrm{n}, \mathrm{i}) = \frac{R(\theta, \mathrm{n}, \mathrm{i}) - \mu}{\sigma}$$

where i indexes the $N^{th}$ neuron, θ is the stimulation orientation, n is the trial number, $Z(\theta, \mathrm{n}, \mathrm{i})$ is the z-scored response, $R(\theta, \mathrm{n}, \mathrm{i})$ is the actual $\Delta F/F_0$ response, μ is the mean $\Delta F/F_0$ value over the monocular or binocular recording period, and σ is the standard deviation from the mean $\Delta F/F_0$ value. Template population responses for each stimulation condition (φ) were generated by computing the median across repeated trials to the same stimulus orientation for the z-scored responses. Similarity between the actual trial evoked population vector and each template was defined as:

$$\Theta_\theta(\theta, n) = \frac{\sum_{\mathrm{i}=1}^{\mathrm{n}} \left( Z(\theta, \mathrm{n}, \mathrm{i}) \cdot Template(\varphi, \mathrm{i}) \right)}{\|Z(\theta, \mathrm{n})\| \, \|Template(\varphi)\|}$$

where φ is the stimulus orientation for the template and · indicates multiplication. To ensure our analysis was comparable across different fields-of-view where the number of cells present varies widely, we limited the number of cells to 50 at any time for our decoder. The similarity metric computed for each template was bootstrap resampled without replacement, but a different subset of cells was used for each resampling procedure (n=1,000). The decoded stimulation orientation was defined as the stimulus orientation for the template showing the highest median similarity across bootstrap resampling to the population activity vector.

**Statistics**

Unless otherwise noted, hypothesis testing was performed using either a permutation or bootstrapping test. We deliberately chose to use resampling methods for hypothesis testing, rather than relying on standard parametric or non-parametric tests, to avoid confounds that could arise from making assumptions on the underlying sampling distributions present in our data. Statistical significance was assessed by ranking if the observed difference between group averages (i.e. mean or median) was more extreme than the $95^{th}$ percentile from a surrogate distribution, where the null hypothesis is true. All statistical tests were two-tail, except when assessing if the performance of the normalized template matching decoder was above chance-levels (one-tail). For each hypothesis test, we produced a relevant surrogate distribution by pooling data between groups, bootstrapped new group averages from the pooled data using replacement (n=1,000), and then computed a distribution of differences between surrogate group averages. Unequal group sizes were maintained for unpaired tests, while resampling was restricted between paired measurements for any paired test. Permutation tests were performed similarly, but data was only exchanged between tested groups, rather than resampled with replacement.

**Acknowledgements**

We would like to thank J. Drayer and D. Ouimet for technical and surgical assistance, as well as members of the Fitzpatrick laboratory for helpful discussions. This research was supported by US National Institutes of Health grants EY011488 and EY026273 and the Max Planck Florida Institute for Neuroscience.

**Author contributions**

All authors designed the study, analyzed the results, and wrote the paper. D.W. and J.C. performed the wide-field and 2-photon calcium imaging and contributed equally to this work.

## References


Bednar, J.A., and Miikkulainen, R. (2006). Joint maps for orientation, eye, and direction preference in a self-organizing model of V1. Neurocomputing *69*, 1272-1276.

Bhaumik, B., and Shah, N.P. (2014). Development and matching of binocular orientation preference in mouse V1. Front Syst Neurosci *8*, 128.

Bienenstock, E.L., Cooper, L.N., and Munro, P.W. (1982). Theory for the development of neuron selectivity: orientation specificity and binocular interaction in visual cortex. J Neurosci *2*, 32-48.

Birch, E.E., Li, S.L., Jost, R.M., Morale, S.E., De La Cruz, A., Stager, D., Jr., Dao, L., and Stager, D.R., Sr. (2015). Binocular iPad treatment for amblyopia in preschool children. Journal of AAPOS : the official publication of the American Association for Pediatric Ophthalmology and Strabismus *19*, 6-11.

Blakemore, C., and Van Sluyters, R.C. (1974). Reversal of the physiological effects of monocular deprivation in kittens: further evidence for a sensitive period. The Journal of physiology *237*, 195-216.

Bridge, H., and Cumming, B.G. (2001). Responses of macaque V1 neurons to binocular orientation differences. J Neurosci *21*, 7293-7302.

Cang, J., and Feldheim, D.A. (2013). Developmental mechanisms of topographic map formation and alignment. Annual review of neuroscience *36*, 51-77.

Cang, J., Renteria, R.C., Kaneko, M., Liu, X., Copenhagen, D.R., and Stryker, M.P. (2005). Development of precise maps in visual cortex requires patterned spontaneous activity in the retina. Neuron *48*, 797-809.

Chandrasekaran, A.R., Plas, D.T., Gonzalez, E., and Crair, M.C. (2005). Evidence for an instructive role of retinal activity in retinotopic map refinement in the superior colliculus of the mouse. J Neurosci *25*, 6929-6938.

Chapman, B., and Stryker, M.P. (1993). Development of orientation selectivity in ferret visual cortex and effects of deprivation. J Neurosci *13*, 5251-5262.

Chapman, B., Stryker, M.P., and Bonhoeffer, T. (1996). Development of orientation preference maps in ferret primary visual cortex. J Neurosci *16*, 6443-6453.

Clemens, J.M., Ritter, N.J., Roy, A., Miller, J.M., and Van Hooser, S.D. (2012). The laminar development of direction selectivity in ferret visual cortex. J Neurosci *32*, 18177-18185.

Crair, M.C., Gillespie, D.C., and Stryker, M.P. (1998). The role of visual experience in the development of columns in cat visual cortex. Science *279*, 566-570.

Duhamel, J.R., Colby, C.L., and Goldberg, M.E. (1998). Ventral intraparietal area of the macaque: congruent visual and somatic response properties. J Neurophysiol *79*, 126-136.

Durbin, R., and Mitchison, G. (1990). A dimension reduction framework for understanding cortical maps. Nature *343*, 644-647.

Edelstein, A., Amodaj, N., Hoover, K., Vale, R., and Stuurman, N. (2010). Computer control of microscopes using microManager. Current protocols in molecular biology *Chapter 14*, Unit14 20.

Erwin, E., and Miller, K.D. (1998). Correlation-Based Development of Ocularly Matched Orientation and Ocular Dominance Maps: Determination of Required Input Activities. The Journal of Neuroscience *18*, 9870-9895.

Godecke, I., and Bonhoeffer, T. (1996). Development of identical orientation maps for two eyes without common visual experience. Nature *379*, 251-254.

Goodhill, G.J. (2007). Contributions of theoretical modeling to the understanding of neural map development. Neuron *56*, 301-311.

Gu, Y., and Cang, J. (2016). Binocular matching of thalamocortical and intracortical circuits in the mouse visual cortex. Elife *5*.

Hess, R.F., Mansouri, B., and Thompson, B. (2010). A binocular approach to treating amblyopia: antisuppression therapy. Optometry and vision science : official publication of the American Academy of Optometry *87*, 697-704.
Hyde, P.S., and Knudsen, E.I. (2001). A topographic instructive signal guides the adjustment of the auditory space map in the optic tectum. J Neurosci *21*, 8586-8593.
Issa, N.P., Trachtenberg, J.T., Chapman, B., Zahs, K.R., and Stryker, M.P. (1999). The critical period for ocular dominance plasticity in the Ferret's visual cortex. J Neurosci *19*, 6965-6978.
Kaschube, M., Schnabel, M., Lowel, S., Coppola, D.M., White, L.E., and Wolf, F. (2010). Universality in the evolution of orientation columns in the visual cortex. Science *330*, 1113-1116.
Katz, L.C., and Shatz, C.J. (1996). Synaptic activity and the construction of cortical circuits. Science *274*, 1133-1138.
King, A.J., and Hutchings, M.E. (1987). Spatial response properties of acoustically responsive neurons in the superior colliculus of the ferret: a map of auditory space. J Neurophysiol *57*, 596-624.
Knudsen, E.I., and Brainard, M.S. (1991). Visual instruction of the neural map of auditory space in the developing optic tectum. Science *253*, 85-87.
Knudsen, E.I., and Knudsen, P.F. (1989). Vision calibrates sound localization in developing barn owls. J Neurosci *9*, 3306-3313.
Ko, H., Cossell, L., Baragli, C., Antolik, J., Clopath, C., Hofer, S.B., and Mrsic-Flogel, T.D. (2013). The emergence of functional microcircuits in visual cortex. Nature *496*, 96-100.
Ko, H., Mrsic-Flogel, T.D., and Hofer, S.B. (2014). Emergence of feature-specific connectivity in cortical microcircuits in the absence of visual experience. J Neurosci *34*, 9812-9816.
Kohonen, T. (1988). Self-organized formation of topologically correct feature maps. In Neurocomputing: foundations of research, A.A. James, and R. Edward, eds. (MIT Press), pp. 509-521.
Koulakov, A.A., and Chklovskii, D.B. (2001). Orientation preference patterns in mammalian visual cortex: a wire length minimization approach. Neuron *29*, 519-527.
Levine, J.N., Chen, H., Gu, Y., and Cang, J. (2017). Environmental Enrichment Rescues Binocular Matching of Orientation Preference in the Mouse Visual Cortex. J Neurosci *37*, 5822-5833.
Miller, K.D. (1994). A model for the development of simple cell receptive fields and the ordered arrangement of orientation columns through activity-dependent competition between ON- and OFF-center inputs. J Neurosci *14*, 409-441.
Miller, K.D., Keller, J.B., and Stryker, M.P. (1989). Ocular dominance column development: analysis and simulation. Science *245*, 605-615.
Montijn, J.S., Vinck, M., and Pennartz, C.M. (2014). Population coding in mouse visual cortex: response reliability and dissociability of stimulus tuning and noise correlation. Frontiers in computational neuroscience *8*, 58.
Murphy, K.M., Roumeliotis, G., Williams, K., Beston, B.R., and Jones, D.G. (2015). Binocular visual training to promote recovery from monocular deprivation. Journal of vision *15*, 15 11 12.
Peirce, J.W. (2007). PsychoPy--Psychophysics software in Python. Journal of neuroscience methods *162*, 8-13.
Sarnaik, R., Wang, B.S., and Cang, J. (2014). Experience-dependent and independent binocular correspondence of receptive field subregions in mouse visual cortex. Cereb Cortex *24*, 1658-1670.
Sengpiel, F., Godecke, I., Stawinski, P., Hubener, M., Lowel, S., and Bonhoeffer, T. (1998). Intrinsic and environmental factors in the development of functional maps in cat visual cortex. Neuropharmacology *37*, 607-621.
Shouval, H.Z., Goldberg, D.H., Jones, J.P., Beckerman, M., and Cooper, L.N. (2000). Structured long-range connections can provide a scaffold for orientation maps. J Neurosci *20*, 1119-1128.

Smith, G.B., Hein, B., Whitney, D.E., Fitzpatrick, D., and Kaschube, M. (2018). Distributed network interactions and their emergence in developing neocortex. Nat Neurosci *21*, 1600-1608.
Smith, S.L., and Trachtenberg, J.T. (2007). Experience-dependent binocular competition in the visual cortex begins at eye opening. Nat Neurosci *10*, 370-375.
Stevens, J.L., Law, J.S., Antolik, J., and Bednar, J.A. (2013). Mechanisms for stable, robust, and adaptive development of orientation maps in the primary visual cortex. J Neurosci *33*, 15747-15766.
Trachtenberg, J.T. (2015). Competition, inhibition, and critical periods of cortical plasticity. Current opinion in neurobiology *35*, 44-48.
Triplett, J.W., Owens, M.T., Yamada, J., Lemke, G., Cang, J., Stryker, M.P., and Feldheim, D.A. (2009). Retinal input instructs alignment of visual topographic maps. Cell *139*, 175-185.
von der Malsburg, C. (1973). Self-organization of orientation sensitive cells in the striate cortex. Kybernetik *14*, 85-100.
Wallace, M.T., and Stein, B.E. (1997). Development of multisensory neurons and multisensory integration in cat superior colliculus. J Neurosci *17*, 2429-2444.
Wang, B.S., Sarnaik, R., and Cang, J. (2010). Critical period plasticity matches binocular orientation preference in the visual cortex. Neuron *65*, 246-256.
White, L.E., Coppola, D.M., and Fitzpatrick, D. (2001). The contribution of sensory experience to the maturation of orientation selectivity in ferret visual cortex. Nature *411*, 1049-1052.
Wiesel, T.N., and Hubel, D.H. (1974). Ordered arrangement of orientation columns in monkeys lacking visual experience. The Journal of comparative neurology *158*, 307-318.
Wilson, D.E., Smith, G.B., Jacob, A.L., Walker, T., Dimidschstein, J., Fishell, G., and Fitzpatrick, D. (2017). GABAergic Neurons in Ferret Visual Cortex Participate in Functionally Specific Networks. Neuron *93*, 1058-1065 e1054.
Wolf, F. (2005). Symmetry, multistability, and long-range interactions in brain development. Phys Rev Lett *95*, 208701.
Wolf, F., Bauer, H.U., Pawelzik, K., and Geisel, T. (1996). Organization of the visual cortex. Nature *382*, 306-307.
Yaeger, C.E., Ringach, D.L., and Trachtenberg, J.T. (2019). Neuromodulatory control of localized dendritic spiking in critical period cortex. Nature *567*, 100-104.

## Supplemental Figures

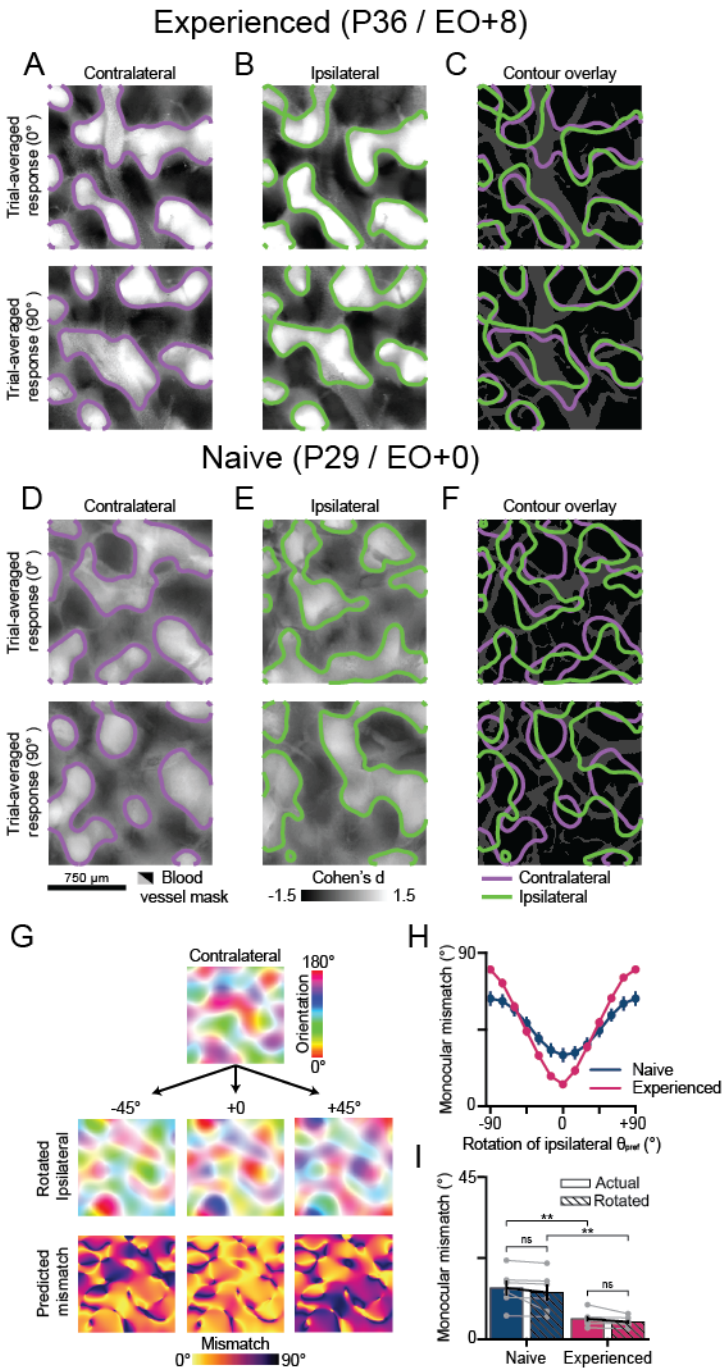


**Supplemental Figure 1: Activity patterns evoked by monocular visual stimuli yield different activity patterns in visually naive animals.**

**(A-B)** Trial-averaged, cocktail-blank subtracted response maps evoked by monocular presentation to drifting gratings for the experienced animal in Figure 1E. Contours denote active domains. Active domains were defined as regions

where the relative activity of z-scored trial-average response maps was >0.25 after applying a 10x10 median filter. **(C)** Contour overlay of the active domains in (A-B). **(D-F)** Same as (A-C), but for the naive experienced animal in Figure 1D. For all widefield images, grayed or blacked out regions represent blood vessels. **(G)** Schematic of rotating the ipsilateral preferred orientation map relative to the contralateral preferred orientation mapn. **(H)** The effect that rotating the preferred orientation of the ipsilateral eye has on the monocular mismatch in widefield imaging across naive and experienced animals (mean±SEM). **(I)** The widefield monocular mismatch before and after rotating the ipsilateral orientation preference map to minimize the monocular mismatch. Gray and black dots respectively reflect individual or grouped measurements. Asterisks denote significance between groups (ns: $p>0.05$, **:$p<0.01$). Animal experiments: naive (n=6) and experienced (n=7).

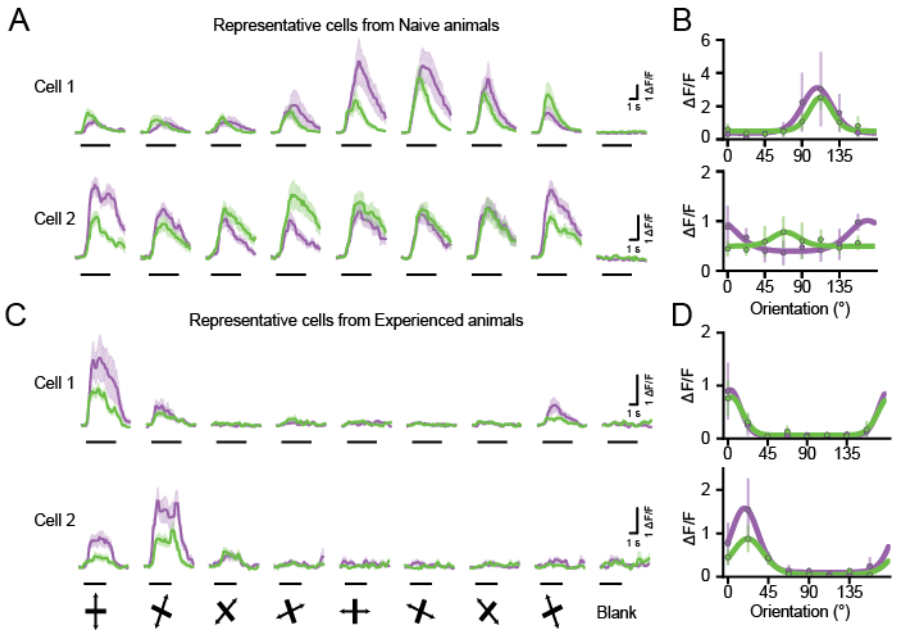


**Supplemental Figure 2: Additional examples of cellular responses in visually naive and experienced animals**

**(A)** Representative cellular response traces from naive animals (mean±SEM). The line under each response trace indicates visual stimulation period. **(B)** For cells in (A), the trial-average responses (median±MAD) and fit orientation tuning curves. **(C-D)** Same as (A-B), but for cells from experienced animals.

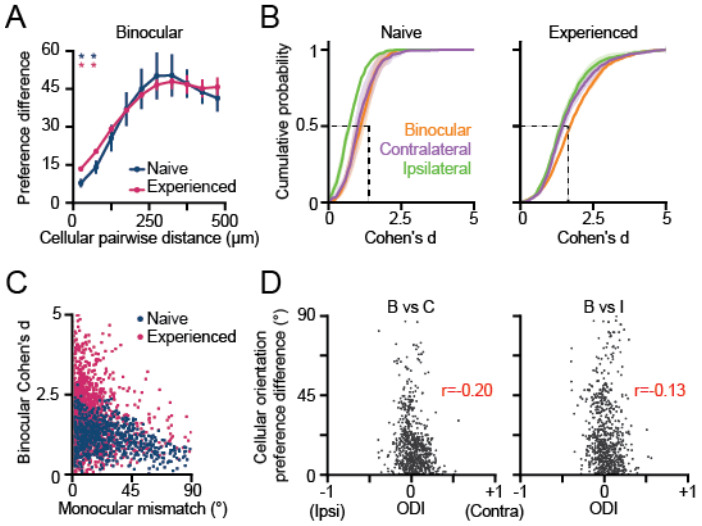


**Supplemental Figure 3: Additional analyses of the binocular and naive responses**

**(A)** Distance-dependent, cellular clustering of the binocular preferred orientation for naive and experienced animals (mean±SEM). **(B)** Cumulative distributions of binocular and monocular orientation selectivity (Cohen's d) for naive and experienced animals (mean±SEM). **(C)** Scatter plot of the cellular monocular mismatch and binocular selectivity (Cohen's d) for naive and experienced animals. **(D)** Scatter plots of ODI and the orientation preference difference of the binocular preferred orientation with either monocular preferred orientation. The Pearson's correlation coefficient (r) is listed in the figure panel. Animal experiments: naive (n=3 animals) and experienced (n=3 animals).

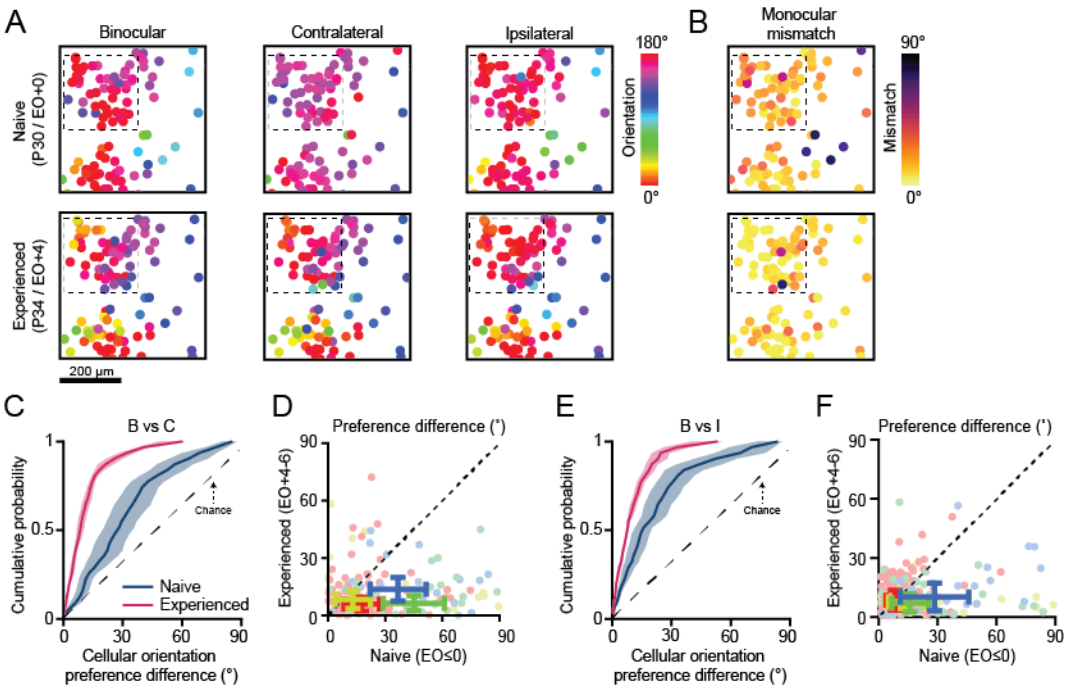


**Supplemental Figure 4: Additional quantification of binocular matching in chronically tracked cells**

**(A-B)** Representative cellular orientation preference maps (A) and monocular mismatch maps (B) for chronically tracked cells before (top row) and after (bottom row) eye-opening. Circles are cells and color represents either the preferred orientation or monocular mismatch. **(C)** Cumulative distributions of orientation preference difference of the binocular and contralateral preferred orientations for chronically tracked cells before and after eye-opening (mean±SEM, n=4 animals). **(D)** Scatter plot of the orientation preference difference of the binocular and contralateral preferred orientations for chronically tracked cells before and after eye-opening. The error bars represent the Median±MAD for each animal experiment (n=4 animals), while the color of each dot or error bar represents the animal experiment. **(E-F)** Same as (C-D), but for the orientation preference difference of the binocular and ipsilateral preferred orientations.

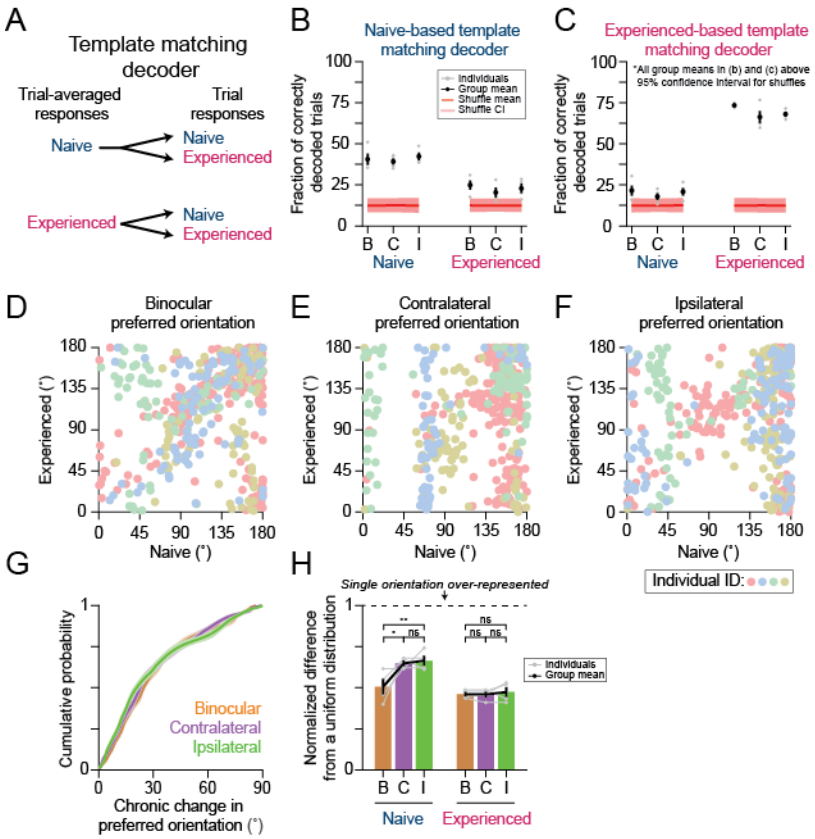


**Supplemental Figure 5: Additional quantification of chronically tracked cells**

**(A)** Template-matching decoder schematic for chronically tracked cells. **(B)** Fraction of correctly decoded trials to binocular and monocular stimulation before and after eye-opening using decoder templates generated before eye-opening (mean±SEM). **(C)** Same as (B), but using decoder templates generated after eye-opening. **(D-F)** Scatter plot of the binocular (D), contralateral (E), and ipsilateral (F) preferred orientations for chronically tracked cells before and after eye-opening. **(G)** Cumulative distributions of orientation preference difference across time for chronically tracked cells before and after eye-opening (mean±SEM). **(H)** Normalized average difference of the distribution of preferred orientations in a cellular field-of-view from a uniform distribution of preferred orientation (mean±SEM). Gray and black lines/dots in (B-C, H) reflect either individual or grouped measurements (n=4 animals), while asterisks denote significance between groups (*:p<0.05,**:p<0.01, ns: p>0.05).

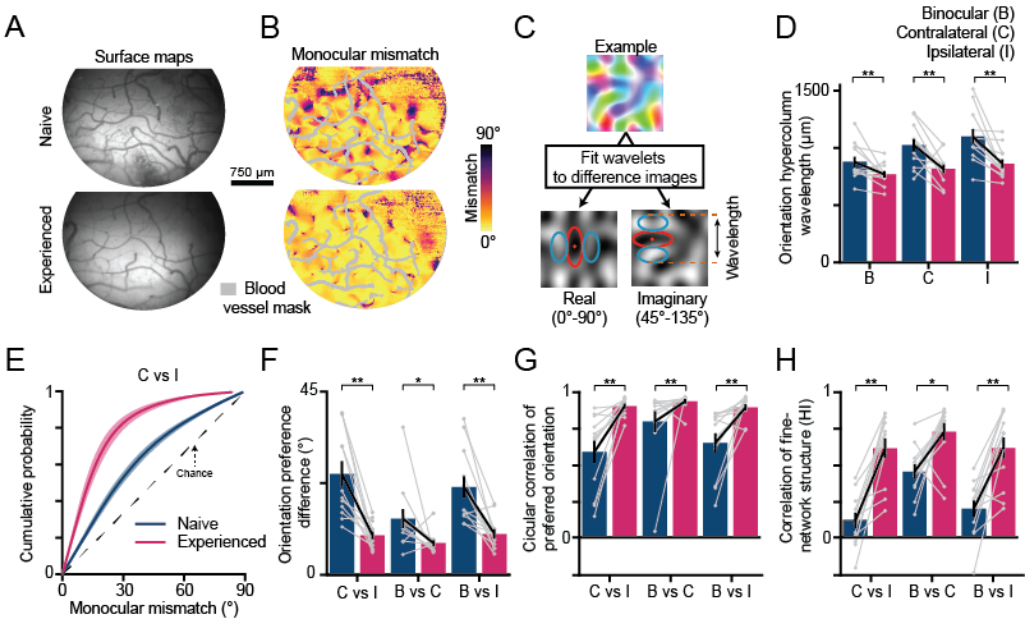


**Supplemental Figure 6: Additional quantification of chronic widefield data**

**(A)** The chronically tracked region before and after eye-opening for the case in Figure 6. **(B)** The monocular mismatch map for (A). Monocular mismatch is represented by image color, while grayed out regions represent blood vessels. **(C)** Schematic of fitting wavelets to response maps to measure orientation hypercolumn size. **(D)** Mean orientation hypercolumn size for chronically tracked monocular and binocular orientation preference maps before and after eye-opening (mean±SEM). Gray and black dots respectively reflect individual or grouped measurements (n=12 animals), while asterisks denote significance differences across time (*:p<0.05,**:p<0.01, ns: p>0.05). **(E)** Cumulative distributions of monocular mismatch across time for chronically tracked animals (mean±SEM). **(F-H)** Similar to (D), but comparing the orientation preference difference (F), circular correlation of the preferred orientation (G), and Pearson's correlation of fine-network structure (H) of the binocular and monocular orientation maps.